JGR Space Physics

RESEARCH ARTICLE

10.1029/2024JA032578

Observation of Quiet-Time Mid-Latitude Joule Heating and Comparisons With the TIEGCM Simulation

E. K. Day[1], A. Grocott[1], M.-T. Walach[1], J. A. Wild[1], G. Lu[2], J. M. Ruohoniemi[3], and A. J. Coster[4]

[1]Lancaster University, Lancaster, UK, [2]National Center for Atmospheric Research, High Altitude Observatory, Boulder, CO, USA, [3]Virginia Polytechnic Institute and State University, Blacksburg, VA, USA, [4]MIT Haytstack Observatory, Westford, MA, USA

Key Points:

- Observations from a Fabry-Perot interferometer and Super Dual Auroral Radar Network radar were used to estimate quiet-time mid-latitude Joule heating rates during 16 July 2014
- The neutral winds accounted for between 24% and 43% of the total observed local Joule heating rates
- Joule heating enhancements were observed approximately 8 times higher than modeled by the Thermosphere Ionosphere Electrodynamic General Circulation Model due to excitations in sub-auroral ion motion

Correspondence to:

A. Grocott,
a.grocott@lancaster.ac.uk

Citation:

Day, E. K., Grocott, A., Walach, M.-T., Wild, J. A., Lu, G., Ruohoniemi, J. M., & Coster, A. J. (2024). Observation of quiet-time mid-latitude Joule heating and comparisons with the TIEGCM simulation. *Journal of Geophysical Research: Space Physics*, *129*, e2024JA032578. https://doi.org/10.1029/2024JA032578

Received 23 FEB 2024
Accepted 6 AUG 2024

Author Contributions:

Conceptualization: E. K. Day, A. Grocott
Data curation: J. M. Ruohoniemi, A. J. Coster
Formal analysis: E. K. Day, A. Grocott, G. Lu
Funding acquisition: A. Grocott
Investigation: E. K. Day, A. Grocott, M.-T. Walach, J. A. Wild
Methodology: E. K. Day, A. Grocott, M.-T. Walach, J. A. Wild, G. Lu
Project administration: A. Grocott
Resources: A. Grocott
Software: E. K. Day
Supervision: A. Grocott, M.-T. Walach, J. A. Wild
Validation: E. K. Day
Visualization: E. K. Day

Abstract Joule heating is a major energy sink in the solar wind-magnetosphere-ionosphere system and modeling it is key to understanding the impact of space weather on the neutral atmosphere. Ion drifts and neutral wind velocities are key parameters when modeling Joule heating, however there is limited validation of the modeled ion and neutral velocities at mid-latitudes. We use the Blackstone Super Dual Auroral Radar Network radar and the Michigan North American Thermosphere Ionosphere Observing Network Fabry-Perot interferometer to obtain the local nightside ion and neutral velocities at ∼40° geographic latitude during the nighttime of 16 July 2014. Despite being a geomagnetically quiet period, we observe significant sub-auroral ion flows in excess of 200 ms^{-1}. We calculate an enhancement to the local Joule heating rate due to these ion flows and find that the neutrals impart a significant increase or decrease to the total Joule heating rate of >75% depending on their direction. We compare our observations to outputs from the Thermosphere Ionosphere Electrodynamic General Circulation Model (TIEGCM). At such a low geomagnetic activity however, TIEGCM was not able to model significant sub-auroral ion flows and any resulting Joule heating enhancements equivalent to our observations. We found that the neutral winds were the primary contributor to the Joule heating rates modeled by TIEGCM rather than the ions as suggested by our observations.

Plain Language Summary Charged particle motion in Earth's upper atmosphere creates heating called Joule heating which causes the atmosphere to expand, increasing drag for objects and satellites. Charged particle velocities are typically greater at high-latitudes than mid and lower latitudes. At mid and lower latitudes, Earth's neutral atmosphere can move faster than the charged particles and produce Joule heating. We can use ground based instruments to observe this particle motion and estimate the Joule heating. Physical models can estimate the Joule heating for different space weather conditions. These physical models show good estimations of the high-latitude Joule heating compared to estimations, however there is limited validation of their performance at mid-latitudes. We use ground based instruments to estimate the Joule heating over mid-latitude North America for one night and compare to outputs from a physics model called the Thermosphere Ionosphere Electrodynamic General Circulation Model (TIEGCM). Despite quiet driving conditions, we observe significant charged particle motion driving enhanced Joule heating rates. We find that TIEGCM was unable to model these strong charged particle motions nor any Joule heating enhancements equivalent to our observations. While the observed heating resulted from faster charged particle motion, the Joule heating rates in TIEGCM were produced by the greater neutral winds instead of ion drifts.

1. Introduction

A significant fraction of the energy flowing through the magnetosphere-ionosphere system is lost to the atmosphere via Joule heating, which in the ionosphere-thermosphere system can be equated to frictional heating between charge carriers and neutral constituents within Earth's upper atmosphere (Vasyliunas & Song, 2005). Joule heating is the dominant magnetosphere-ionosphere energy input source, typically responsible for twice as much energy input compared to auroral power (Knipp et al., 2004; Lu et al., 1996, 1998, 2016) and up to 70% of the total ionospheric power input during geomagnetic storms (Knipp et al., 2004). This heating can cause ionospheric and thermospheric expansion (Fuller-Rowell et al., 1997; Lu et al., 2016; Knipp et al., 1998; Rishbeth et al., 1969; S. R. Zhang et al., 2017) which can result in enhanced ion outflow (Wahlund et al., 1992) and increased satellite drag that can reduce operational lifetime (Dang et al., 2022; Fang et al., 2022; Lin et al., 2022). It is therefore important that we understand the causes of Joule heating across all regions of the ionosphere.

Writing – original draft: E. K. Day, A. Grocott, M.-T. Walach, J. A. Wild
Writing – review & editing: E. K. Day, A. Grocott, M.-T. Walach, J. A. Wild, G. Lu, J. M. Ruohoniemi, A. J. Coster

Joule heating has been extensively studied at the high-latitudes (Kiene et al., 2019; Wang et al., 2020). Ion motion is controlled by magnetic reconnection between the interplanetary magnetic field (IMF) and Earth's magnetosphere, circulating due to $\vec{E} \times \vec{B}$ drift antisunwards at polar latitudes then returning sunwards at lower latitudes (Cowley & Lockwood, 1992; Dungey, 1961) under southwards IMF conditions. Motion of the neutrals in the thermosphere is driven by a combination of solar pressure gradients, coriolis forces and drag from ion motion (Rishbeth, 1977). Typically at high-latitudes, neutral velocities are small relative to the ion velocities such that Joule heating is primarily due to motion of the ions. High-latitude Joule heating calculations have therefore often discounted contributions from the neutrals. However during non-storm times and at lower latitudes, the velocities of the neutrals relative to the ions can be significant. Using model simulations, Lu et al. (1995) calculated the neutrals to have an approximate 28% negative effect on Joule heating. Often the neutral velocities at mid-latitudes can exceed the ion velocities. Both Zou and Nishitani (2014) and Joshi et al. (2015) used Super Dual Auroral Radar Network (SuperDARN) data to show that neutral motion driven by expanded $\vec{E} \times \vec{B}$ ion drift due to intense geomagnetic storms can persist up to 20 hr after the recovery phase, resulting in neutral wind driven mid-latitude ion motion known as the disturbance dynamo effect. A study by Billett et al. (2018) focusing on the high-latitudes used a combination of SuperDARN and neutral wind model data to find that global Joule heating patterns have a significant dependence on UT due to neutral wind enhancements. Studies including the mid-lower latitudes and during periods of weaker geomagnetic activity must therefore include neutral wind contributions when calculating the Joule heating.

Joule heating is calculated as the dissipation rate of currents perpendicular to the magnetic field, $\vec{J_\perp} \cdot \vec{E}$ (Lu et al., 1995) and the total Joule heating rate can be calculated with Equation 1 (Baker et al., 2004),

$$\vec{J_\perp} \cdot \vec{E}_\perp = \sigma_p \left(\vec{E} + \vec{V_n} \times \vec{B}\right)^2 \tag{1}$$

where $\vec{E} = -\vec{V_i} \times \vec{B}$ is the electric field in the Earth's reference frame due to the ion motion, $\vec{V_i}$, assuming a stationary neutral background, σ_p is the conductivity in the direction of the electric field (Pedersen conductivity), $\vec{V_n}$ is the velocity of the background neutrals and $\vec{B}$ is the magnetic field strength. $\vec{V_n} \times \vec{B}$ accounts for the electric field generated by the neutral wind dynamo due to the drag imposed on charged particles in the ionosphere.

Equation 1 can be expanded into Equation 2 (Billett et al., 2018) which conveniently breaks it down into the three terms that individually describe the main contributors to the total Joule heating.

$$Q_j = \overbrace{\sigma_p E^2}^{Q_i} + \overbrace{\underbrace{2\sigma_p \vec{E} \cdot \left(\vec{V_n} \times \vec{B}\right)}_{Q_{w1}} + \underbrace{\sigma_p \left(\vec{V_n} \times \vec{B}\right)^2}_{Q_{w2}}}^{Q_w} \tag{2}$$

Q_i is the ion heating and is the heating that would be generated by ions moving against a stationary neutral background. Q_{w1} is the first wind correction term and accounts for the direction of the ions relative to the neutrals. If the neutrals and ions move in the same direction then the difference between their velocities is smaller and the frictional heating due to collisions between the neutrals and ions will be lower. Conversely, if they move in opposing directions the difference in their velocities will be greater and the heating will be larger, therefore Q_{w1} can act to either increase or decrease the total Joule heating. Q_{w2} is the heating that would be generated by the neutrals moving against a stationary ion background. Together, Q_{w1} and Q_{w2} create the wind correction term Q_w, which describes the total heating accounted for by motion of the neutral wind relative to the ions.

Except for geomagnetic storms, where the twin cell $\vec{E} \times \vec{B}$ convection pattern expands to 40° magnetic latitude (Walach & Grocott, 2019; Walach et al., 2021) from its high-latitude (>60° magnetic latitude) boundary, most ion flows at the mid-latitudes (40°–60° magnetic latitude) are sub-auroral. At sub-auroral latitudes, ion motion is often associated with sub-auroral polarization streams (SAPS) (Billett et al., 2022; Clausen et al., 2012), penetrating electric fields (Maimaiti et al., 2018, 2019) and pressure gradient drifts (Greenwald et al., 2006; Hudson & Kelley, 1976; Liu et al., 2021) that are mostly responsible for driving subauroral ion flows. Billett et al. (2022)

observed significant equatorward and westward neutral wind disturbances during a SAPS event. They found that the response of the neutrals close to the SAPS was almost immediate and was likely driven by ion neutral coupling. They did however also find neutral disturbances further from the SAPS after a 2 hr time lag that they propose were due to pressure gradient and Coriolis forces from the SAPS heating. The difference in neutral response due to location indicates the importance of considering the mesoscale structure of ionospheric events when accounting for neutral particle motion. Furthermore a study by Kiene et al. (2019) found that the difference in high-latitude Joule heating rates varied by as much as a factor of 10 due to local variations in the observed ion-neutral structure. If we are to accurately estimate the Joule heating rate during ionosphere-thermosphere disturbances it is then necessary to ensure that the ion and neutral measurements are as colocated as possible.

The Blackstone (BKS) Super Dual Auroral Radar Network (SuperDARN) radar and the Ann Arbor (ANN) North American Thermosphere Ionosphere Observation Network (NATION) interferometer are two mid-latitude ground-based instruments, used for observing ion and neutral flows in the F-region of the ionosphere respectively, (see Section 2) whose fields of view (FOV's) overlap each other, allowing for colocated observations of mid-latitude ion and neutral flows. As the majority of ion motion at the mid-latitudes occur during quiet periods we search for quiet time coincident ion and neutral observations. Identifying times of high-quality colocated observations during quiet times is extremely difficult. Both instruments need to be operational, the BKS radar needs to observe ionospheric scatter during the nighttime period in the region over the FPI and the ANN FPI needs to have suitable (uncloudy) observation conditions. Intervals where all these requirements are satisfied are unfortunately rare. Nevertheless we have identified the nighttime of 16 July 2014 as a period where all the necessary conditions are met, allowing us to study the local quiet-time mid-latitude Joule heating during this interval.

Global circulation models are often used to study high-latitude ionosphere-thermosphere and Joule heating processes (Lu et al., 2016; Wang et al., 2020), however a lack of studies using global models focused on the mid-latitudes leaves some uncertainty in their reliability to provide accurate mid-latitude modeling. We therefore compare our ion and neutral observations and Joule heating estimations with equivalent outputs from the Thermosphere Ionosphere General Circulation Model (TIEGCM, see Section 2). This paper is split into the following sections: Section 2 details the observed and modeled data used in this study, Section 3 provides an overview of the geomagnetic conditions and observations made during the night of 16 July 2014. Section 4 details the methods used to estimate the Joule heating rate while presenting the results of those estimations. Finally, Section 5 discusses the results in context of the wider literature and scientific community.

2. Parameters and Models

2.1. Ion Motion

The Super Dual Auroral Radar Network (SuperDARN) (Chisham et al., 2007; Greenwald et al., 1995; Nishitani et al., 2019) is a series of high frequency radars in the northern and southern hemispheres that provide observations of ionospheric dynamics across high and mid-latitudes. In the northern hemisphere, SuperDARN comprises radars which have near total hemispheric coverage of the polar, high-latitude and mid-latitude regions. For this investigation we consider data from the Blackstone (BKS) radar due to its field of view (FOV) overlapping the FPI used in this study (see Section 2.2). Each radar can electronically steer its look direction, centered on which it forms a beam typically 3° wide and consisting of 75–100 range gates with a 45 km range resolution. Each radar can sweep through 16–24 beams with the FOV being roughly 50° where a full azimuthal scan across all beams takes 1–2 min.

SuperDARN radars detect field-aligned plasma irregularities in the E and F regions of the ionosphere by recording the backscattered signal from decameter scale electron density structures. Plasma irregularities in the F region drift with $\vec{E} \times \vec{B}$ velocities and their Doppler shift can be used to infer properties of the ionosphere. Due to refraction, the radar beam can reflect off of the ground, known as groundscatter. Groundscatter is typically characterized by a velocity of only a few ms^{-1} and produces a low spectral width, which is often sufficient to distinguish between ionospheric and ground scatter at the high-latitudes. At the mid-latitudes however, and particularly during periods of low geomagnetic activity, ionospheric scatter can often be much slower while exhibiting low spectral widths and these techniques can often eliminate observations of relevant ion motion. Instead we use the algorithm developed by Ribeiro et al. (2011, 2012) which has been specifically designed for identifying mid-latitude ionospheric scatter. The algorithm uses a 3 × 3 × 3 beam by range gate by scan boxcar filter that identifies individual clusters of scatter connected by range gate and scan and determines the ratio of fast to slow moving scatter within each cluster. Errors associated with the filtered velocities are derived using the method described by Ruohoniemi and Baker (1998), however we have modified the method so that velocities are removed if they are two median absolute deviations (Howell, 2005) from the median instead of two standard deviations from the mean. This reduces the impact of unphysical outliers that result in excessive standard deviations due to the lower velocities associated with the mid-latitudes. Since an individual cluster of returned scatter can usually be attributed to either ionospheric backscatter or groundscatter, the algorithm identifies and marks which clusters contain ionospheric scatter. The Ribeiro et al. (2011) algorithm also automatically excludes backscatter from ranges within 315 km of the radar to eliminate scatter originating from the E-region and meteor echoes at near ranges. Furthermore, in this study we modify the algorithm such that it can consider clusters spanning multiple beams similar to A. G. Burrell et al. (2018). This whole approach enables a quantitative ionospheric/groundscatter classification of mid-latitude backscatter.

2.2. Neutral Wind Motion

The North American Thermosphere Ionosphere Observing Network (NATION) (Makela et al., 2012) was a network of five Fabry-Perot Interferometers that observed the neutral wind velocity and temperature in Earth's thermosphere across the mid and eastern parts of the United States of America. Each FPI observes the Doppler shift of the 630 nm OI emission line that is assumed to peak at an altitude of 250 km. The FPIs scan at an elevation angle of 45° and take measurements in the geographic cardinal directions (north, east, south, west) and the Zenith through the nighttime period. Data are analyzed using the techniques described in Harding et al. (2014) to produce estimates of the horizontal neutral winds at ~250 km altitude.

Of the five FPIs in NATION, and assuming that the cardinal measurement locations are located at the peak emission altitudes, we only use data from the Michigan (ANN) instrument due to it being the only FPI that has all of its measurement locations intersecting with the BKS radar's FOV.

2.3. Geomagnetic Field

The 13th generation International Geomagnetic Reference Field (IGRF) model (Alken et al., 2021) profiles the Earth's tilted dipole as a function of time, geographic position and altitude. At high-latitudes, the magnetic field is mostly vertical, however at mid-latitudes and lower, there can be a significant tilt to the angle of the field that needs to be accounted for when comparing the electric field generated by the neutral wind dynamo $\left(\vec{V_n} \times \vec{B}\right)$ with the electric field that is calculated from $\vec{E} \times \vec{B}$ drift, due to the difference in angle between the ion and neutral velocity vectors. The IGRF13 model provides the declination and inclination of the magnetic field at the ANN FPI's location, which at 250 km altitude are $-6.49°$ and $69.26°$ respectively. This inclination and declination do not change significantly between assumed peak emission locations so we do not consider it in our calculations.

2.4. Auroral Boundary

Due to the mid-latitude location this study focuses on, it is important to identify if any observed ion flows are sub-auroral. It has been shown that the boundary between the region 1 and region 2 currents serve as a good approximation for the extent of the equatorward boundary of the auroral oval, particularly on the duskside in the northern hemisphere (Kilcommons et al., 2017). The Active Magnetosphere and Planetary Electrodynamics Response Experiment (AMPERE) uses magnetometers on the Iridium constellation of telecommunication satellites to provide field aligned current measurements across both hemispheres. A spherical harmonic fit to the measured radial current densities alongside Ampere's law (B. J. Anderson et al., 2000; Coxon et al., 2018) produces 10-min cadence global current density maps which can be used to determine the location of the Region 1 and 2 currents, where we use the boundary between them as a proxy for the boundary of the auroral oval.

2.5. Total Electron Content

The mid-latitude ionospheric trough plays a significant role in ionospheric processes in the mid-latitudes (P. C. Anderson et al., 1993; Kunduri et al., 2021; Liu et al., 2021) and can be identified using Total Electron Content (TEC) measurements from Global Positioning System (GPS) data. We use the TEC data to further investigate the mid-latitude dynamics through identification of the trough. The TEC data are processed using the algorithms from

Rideout and Coster (2006) and Vierinen et al. (2016). The TEC data are placed into 1° × 1° geographic latitude by geographic longitude cells integrated over 5 min. Furthermore we median filter the TEC data as described by Thomas et al. (2013) to reduce the geospatial noise among the data set.

2.6. TIEGCM

The Thermosphere Ionosphere Electrodynamic Circulation Model (TIEGCM) (Qian et al., 2014; Richmond et al., 1992) is one of the most widely used thermosphere/ionosphere models within the upper atmospheric scientific community and is a fully three-dimensional time dependent model of Earth's ionosphere and thermosphere that solves the equations of continuity, energy and momentum for the three major ion and neutral species.

TIEGCM uses either the Weimer (2005) or Heelis et al. (1982) electric field models as a driver for the $\vec{E} \times \vec{B}$ driven high-latitude ion convection and can operate using a 5° × 5° or 2.5° × 2.5° resolution in latitude and longitude. Wu et al. (2017) compared TIEGCM's high-latitude thermospheric winds and ion drifts using the two electric field models to observational data and found that using the Weimer model produces more accurate simulations. In this study we run TIEGCM with the Weimer electric field model at a resolution of 2.5° × 2.5°. When using the Weimer electric field model TIEGCM takes the f10.7 solar radio flux, IMF By, IMF Bz, solar wind velocity and solar wind density as input drivers for the model.

TIEGCM produces estimates of the geographic meridional, zonal and vertical ion and neutral velocities at the specified run resolution. Outputs from TIEGCM in this study are taken at an altitude of 250 km, which corresponds to the altitudes of the ion and neutral observations. As the ion and neutral line of sight velocities show little difference between assumed peak emission locations, we simply use the TIEGCM ion and neutral velocities located at the FPI location.

TIEGCM also models the Pedersen conductivity, which we use for calculating both the observational and modeled Joule heating values. Keeping the Pedersen conductivity consistent between observed/modeled methods allows us to better isolate the effect from differences between the observed and modeled ion and neutral velocities, which is the aim of this study.

3. Event Overview

In this section, we present observations from 16 July 2014. First, we present an overview of the geomagnetic conditions, before looking in detail at the ion and neutral velocity observations.

3.1. Geomagnetic Conditions

Geomagnetic conditions during this interval were quiet. Figure 1 shows the interplanetary and geomagnetic conditions, IMF By, IMF Bz, SYM-H, ASYM-H, and Kp during the hours 00:00–10:00 UT. Panel 1a shows the solar wind speed while 1b presents the y and z components of the IMF. Of particular note is the slight negative IMF Bz between 04:00 and 07:00 UT indicating a southwards directed IMF, allowing magnetic reconnection to occur between the IMF and Earth's magnetic field. Panel 1c shows the auroral indices with significant enhancements to the AL, AU and derived AE index coincident with the period of southwards IMF, indicating an increased intensity of the auroral electrojet. Similarly, the SYM-H index (1d) shows an increase in ring current intensity from 05:00 UT while the ASYM-H index (1e) shows an increase in asymmetries in the ring current. Figure 1f shows the Kp index of between 1.7 and 2.3, which indicates minor geomagnetic activity during this period.

3.2. Radar Observations

Figure 2a shows the IMF Bz followed by panels presenting measurements of ionospheric ion velocities for selected beams of the BKS SuperDARN radar between 00:00 and 10:00 UT, specifically beams 15 (b), 17 (c), 7 (d), 9 (e) and 17 (f) which are the beams that intersect through the FPI north, east, south, west and zenith assumed peak emission locations respectively. Negative velocities indicate line of sight ion motion away from the radar and positive velocities toward the radar. The velocity magnitude is given by the colorbar on the right. Portions of the observations that have been determined to be groundscatter according to the Ribeiro et al. (2011, 2012)

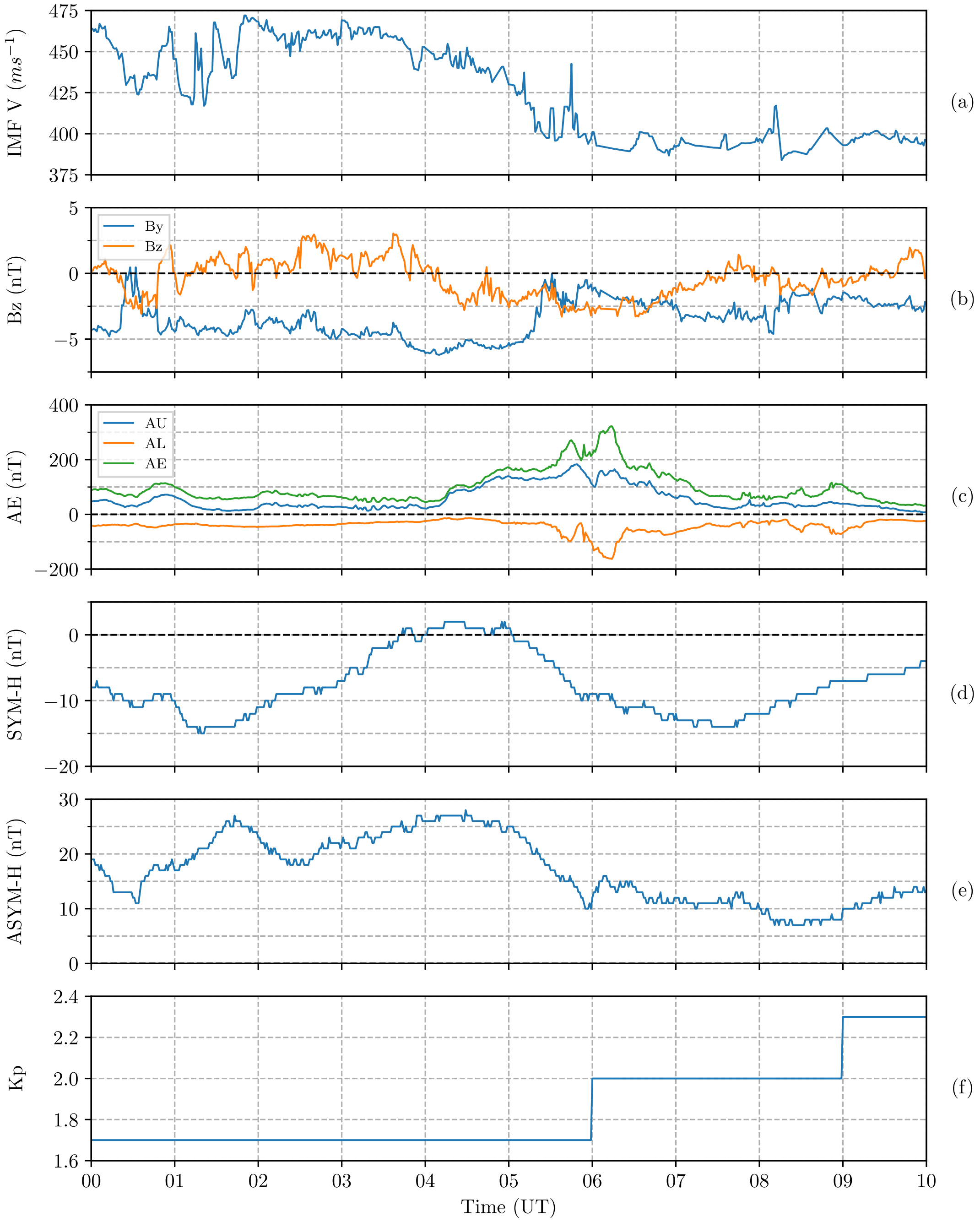

Figure 1. Geomagnetic conditions recorded during the nighttime interval (00:00–10:00 UT) of 16 July 2014. (a) Shows the IMF solar wind speed, v, (b) the IMF magnetic field strength in the y and z directions (c) the AU, AL, and AE indices, (d) the SYM-H index, (e) the ASYM-H index and (f) the three hourly Kp index.

algorithm have been marked in gray. The horizontal dashed lines across each beam range gate panel show the range gate where the assumed peak FPI emission point is located, calculated using the standard SuperDARN virtual height model. Across all beam range gate panels we observe enhancements of the ion velocities during the southwards IMF Bz interval between 04:00 and 07:00 UT, with the most persistent flows traversing the southern and western part of the FPI region (panels d and e). The observed flows exceed -100 ms^{-1}. At high-latitudes, these flows may not be considered to be particularly strong, but at mid-latitudes and especially during periods of low geomagnetic activity such as this, these magnitudes particularly stand out from the background quiet time velocities of typically less than 20 ms^{-1} magnitude. Beams 15 and 17 show positive flows >40 ms^{-1} between

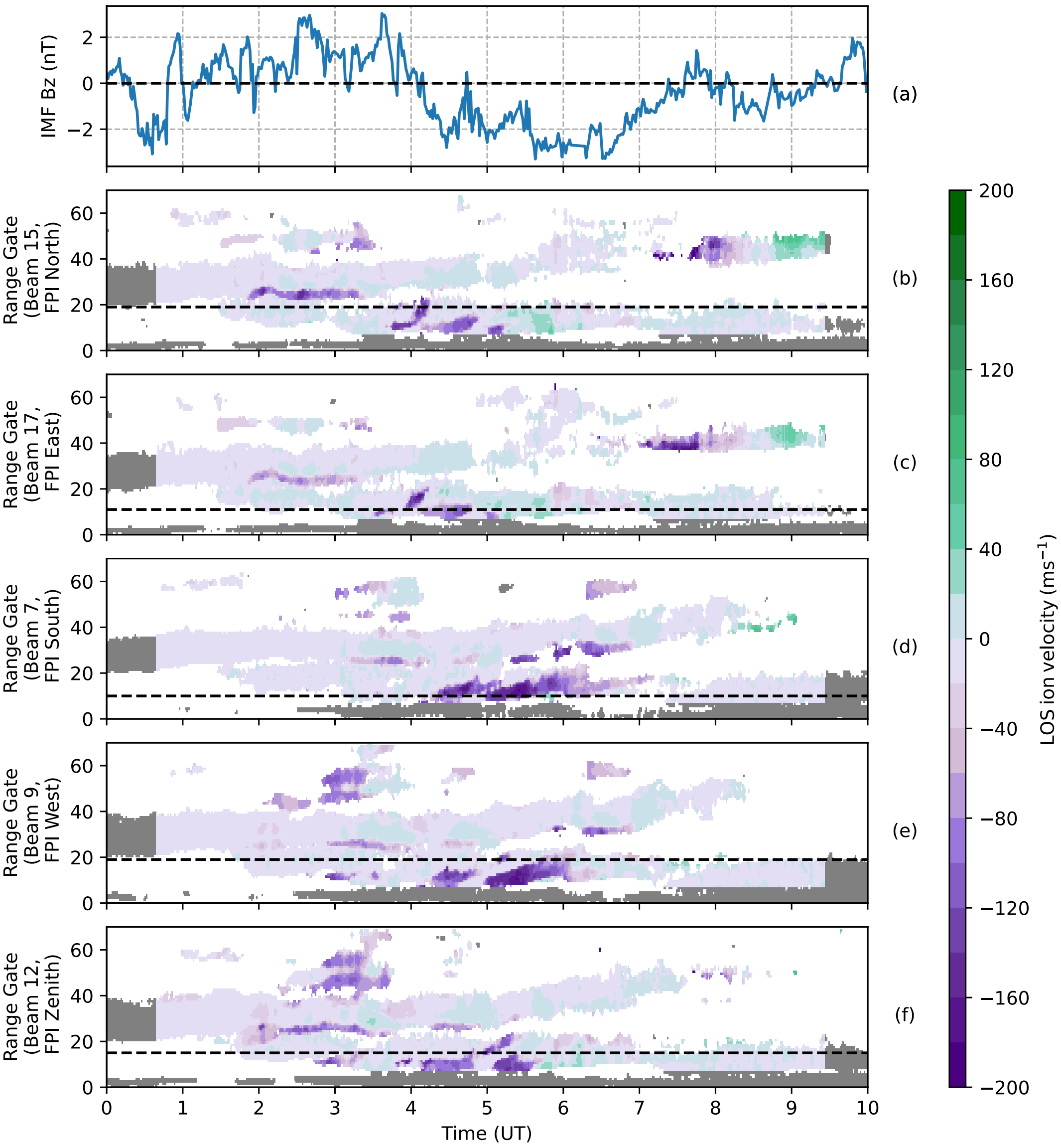

Figure 2. Panels (a) shows the IMF Bz, followed by range gate, time plots for the BKS radar on 16 July 2014, with beams slicing through the assumed peak emission observation locations of the ANN FPI where beam 15 slices through north (b), 17 east (c), 7 south (d), 9 west (e) and 12 the zenith (f). Line of sight ion velocities follow the colorbar on the right, where positive values indicates motion toward the radar and negative away. Gray values are groundscatter. The dashed horizontal lines represent the range gate where the beam slices through the assumed cardinal peak emission of the ANN FPI.

05:00 and 06:00 UT close to the FPI (panels b and c) emission locations, indicating a change in flow direction during these periods, whereas beams 7 and 9 (panels d and e) show the line of sight ion velocities remaining strongly negative. The flow direction switch only in two adjacent beams indicates that multiple flow channels exist during this interval.

To illustrate the spatial morphology and geographical mapping of the excited ion flows, Figure 3 presents a snapshot of SuperDARN flow data from all the north American mid-latitude radars from 06:00 UT, superimposed with the Total Electron Content (TEC) and field-aligned currents (from AMPERE).

The background of Figure 3 shows the 1° × 1° geographic latitude by longitude height integrated TEC map, colored according to the white-black colorbar on the bottom. Dashed circles represent each 10° of geographic latitude. The AMPERE data set shows the field aligned current densities, given by the blue-red colorscale; upward field aligned currents are in blue and downwards in red. Line of sight ion velocities from all the North American

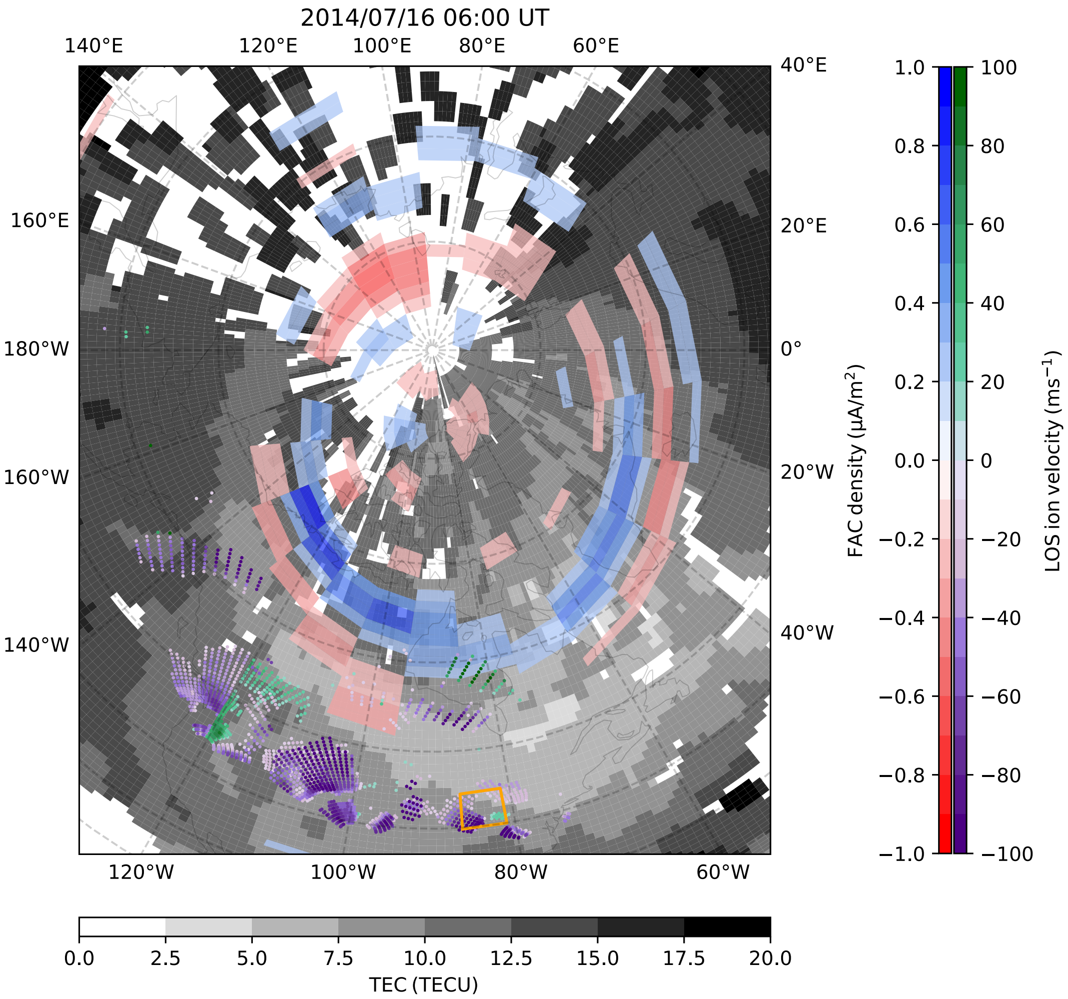

Figure 3. Geographic plot at 06:00 UT 16 July 2016, showing the 1° × 1° latitude × longitude height integrated global total electron content according to the colorscale on the bottom. Dashed lines represent every 10° line of geographic latitude. Also shown is the AMPERE field aligned current density data, binned into 1° magnetic latitude by 1 hr MLT. Upward field aligned currents are given in blue and downwards in red with magnitude according to the red-blue colorbar. Further plotted are line of sight ion velocities from all the north American mid-latitude SuperDARN radars according to the purple-green colorbar, where absolute velocities <15 ms^{-1} have been removed. Note that the line of sight SuperDARN ion velocities are colored so that positive values indicate an eastwards motion and negative a westwards directed flow. Plotted in orange is the box that bounds the FPI cardinal observation locations, where the FPI is located at 01:00 local time in this Figure.

mid-latitude SuperDARN radars are plotted according to the purple-green colorbar, velocities <|15| ms^{-1}, which is the boundary for low/high velocity scatter in the Ribeiro et al. (2011) groundscatter algorithm, have been removed to improve visual clarity. Multiple radars are used in order to identify the spatial extent of the ionospheric scatter over the FPI, given as an orange box at around 85° west, 42° north, which traces the boundaries of the assumed peak neutral wind emission locations. The sign of the SuperDARN ion velocities have been altered from the presentation in Figure 2 such that here positive velocities indicates eastwards directed ion flows and negative westwards.

Figure 3 corresponds to 06:00 UT (01:00 local time at the ANN FPI), chosen due to a strong westwards flow in the south-west region of the FPI area. By tracing a westwards line that starts at 40°N ~ 85°W and finishes at 45°N 105°W, we can see that the strong ion velocities close to the FPI persist through multiple ionospheric scatter ranges and into the FOV of more westwards located radars. The AMPERE data set indicates that the R1/R2 boundary at midnight is between 60° and 50° geographic latitude, approximately 20° poleward of the FPI, we thus conclude that the observed flows are sub-auroral. From the TEC data we can see the formation of the ionospheric

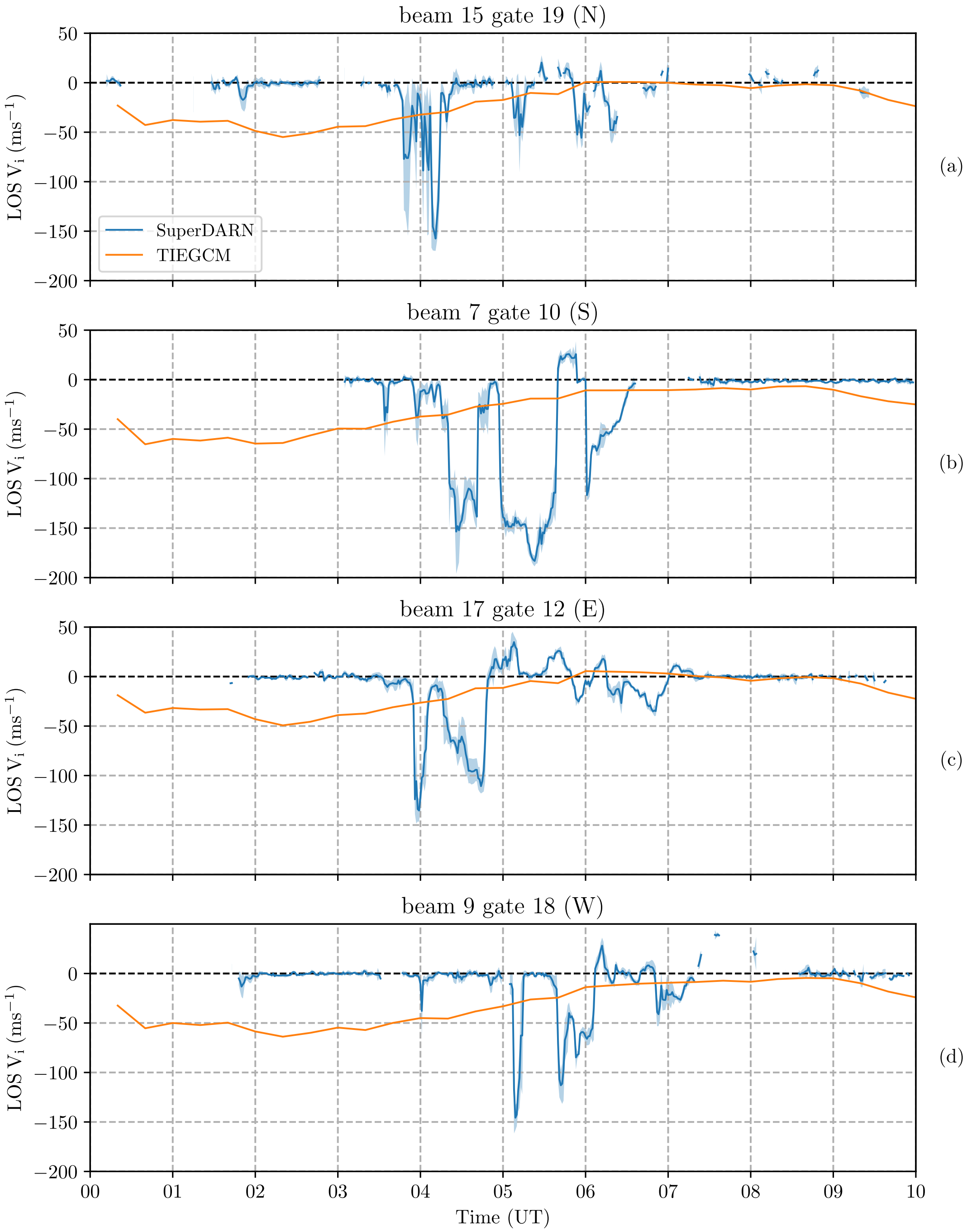

Figure 4. Line of sight ion velocities (blue) recorded from the BKS radar through 00:00–10:00 UT from the beam range-gate cells which overlay the ANN FPI assumed peak emission locations, north (a), south (b), east (c), and west (d). The overlaying FPI assumed peak emission locations for the cardinal directions are also indicated in each panel header. Positive values indicate motion toward the radar and negative away. Shaded regions indicate errors calculated by the method from Ruohoniemi and Baker (1998) but filtering out velocities two median absolute deviations from the median instead of two standard deviations from the mean. Also plotted are the equivalent line of sight ion velocities modeled by TIEGCM (orange).

trough equatorward of the region two currents and poleward of the FPI, starting at ~50° geographic latitude at local midnight and wrapping around to ~70° geographic latitude at the duskside.

A more detailed presentation of the ion flow data from the BKS radar overlooking the ANN FPI is provided by Figure 4, which shows the line of sight velocities for the BKS radar beam range gates that are assumed to contain the cardinal peak emission location of the FPI. Panels, a, b, c, and d are for the beams that slice through the north, south, east and west locations respectively at the range gate that contains the assumed peak emission location. Note, that the panels do not indicate that motion is north/south/east/westwards, instead positive values indicate motion toward the radar and negative away along the azimuth of the radar beam. The recorded line of sight ion velocities are indicated in blue. Shaded regions indicate the errors calculated using the method described in Section 2. Compared in orange are the line of sight velocities from TIEGCM taken at an altitude of 250 km at the same geographic latitude and longitude as the beam range gates and projected into the same direction as the radar beams.

The line of sight velocities show high activity across all beams between 04:00 UT and 07:00 UT. The northern and eastward observations show an early spike at 04:00 UT with line of sight velocities of approximately 160 ms^{-1}. The southern observations show several spikes of high velocities from 04:00 to 06:30 UT peaking at -180 ms^{-1} slightly after 05:30 UT. The westward observations show high velocity spikes occurring between 05:00 and 06:00 UT, peaking at slightly less than -150 ms^{-1}. An interesting observation is that the IMF Bz was directed northwards until after 04:00 UT, however the north and southward BKS radar line of sight measurements show strong flows from as early as 03:30 UT, and the eastwards observation starts to spike just before 04:00 UT, indicating some driver other than the IMF Bz contributed to the fast ion motion. Furthermore, we can see that the westwards spikes begin (~05:10 UT) shortly after the strong eastwards observations end (~04:45 UT), which could indicate that it is the same patch of scatter that traverses across the FOV of the radar. The TIEGCM line of sight resolved ion velocities follow the same general trend over each observation point. Differences between each region can be identified most notably at 05:00 UT, where the east location is around -10 ms^{-1} while the southern point has model velocities of ~ -25 ms^{-1}. There are also slight variations in the magnitudes of the velocities due to the difference in the beam azimuth relative to TIEGCM's modeled three-dimensional ion flows. The TIEGCM line of sight ion velocities hover around their peak value of between 40 and 60 ms^{-1} in all cells from roughly 01:00 to 03:00 UT, well before the first observed ion velocity spikes and southwards directed IMF Bz. They then decrease in velocity to close to 0 ms^{-1} between 0500 UT (for the east observation point) and 07:00 UT (for the south observation point).

3.3. FPI Observations

Figure 5 compares the FPI line of sight velocities (blue) with the neutral velocities modeled by TIEGCM at the assumed peak emission locations (orange). Panels a, b, c and d show the north, south, east and west observation directions respectively. Since TIEGCM's output velocities are given as geographic meridional and zonal magnitudes, we take TIEGCM's meridional flow for the north and south observations and the zonal flow for the east and west observations at each assumed peak emission location. We then project them into the same elevation angle as observed by the FPI. Positive velocities indicate motion to the north (meridionally) and east (zonally). The Zonal directions (east, west) show generally low velocities throughout the nighttime period, the meridional velocities however, show a gradual increase, particularly after the IMF Bz turns southward after 05:00 UT. The north facing observations especially, show a large increase in magnitude up to a peak value of -150 ms^{-1} whereas the south facing observations peak at roughly -80 ms^{-1}. The zonal velocities show similar magnitudes with the East look direction peaking at -30 ms^{-1} and the west look direction at -40 ms^{-1}. Although in our ANN data, the south observations stop after 06:30 UT and a 3 hr data gap occurs in the east observations between 04:00 and 07:00 UT due to the presence of the moon in that direction, the trend in the data between the opposing observation points are similar enough that we can assume that there are no significant changes in the spatial distribution of the neutral wind flows over the ANN FPI. The vertical velocities are shown to fluctuate highly relative to their greatest magnitude, ranging from values of 5 ms^{-1} to -20 ms^{-1}.

When comparing TIEGCM's output, we find that the modeled meridional velocities are similar in magnitude to the observations. At the north location, TIEGCM's neutral velocities are closely aligned with these observations. TIEGCM's velocities at the southern location follow a similar pattern and although the observations stop after 06:00 UT, the trend of increasing magnitude from 02:00 UT is apparent in both the observed and modeled data. The meridional velocities then match well with our observations. Both TIEGCM's velocities at the east and west locations are shown to have a large difference to the observations. Although the trend of a somewhat sinunsoidal variation in both the observed and modeled neutral velocities between 00:00 UT and 09:00 UT, peaking at 05:00 UT, are somewhat similar, TIEGCM's velocities are significantly faster, especially at the peak. TIEGCM is more accurate when estimating the mid-latitude meridional neutral flows than in the zonal direction in this case.

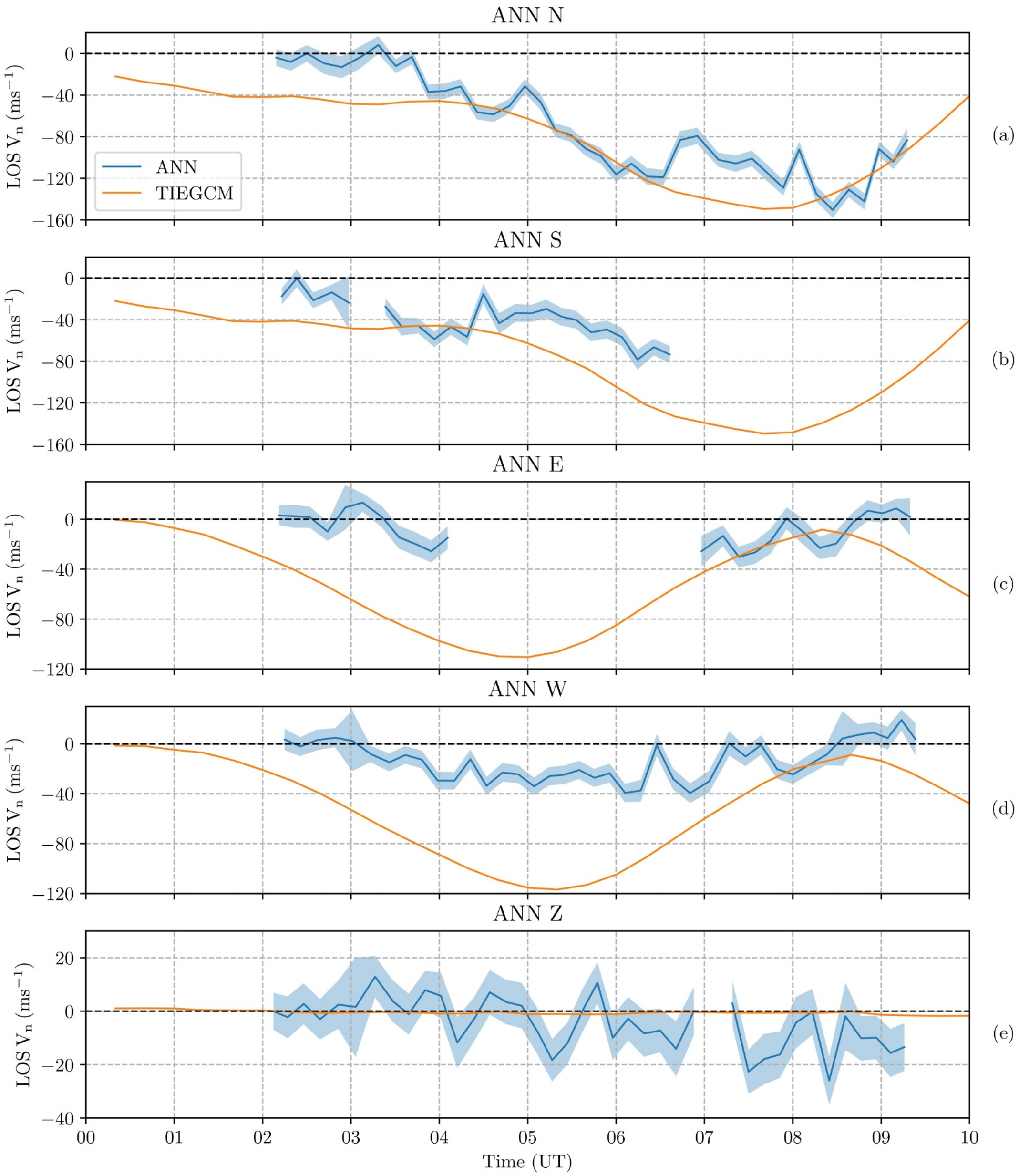

Figure 5. Line of sight neutral velocities recorded by the ANN FPI (blue) through 00:00–10:00 UT for each cardinal observation direction, north (a), south (b), east (c), west (d) and the vertical velocity measured by the zenith (e). Shaded regions show the error in the ANN observations. Positive velocities indicate motion north/east/upwards. Gaps are left where sequential measurements are made more than 20 min apart. Also plotted are the neutral velocities from TIEGCM for the equivalent line of sight locations and directions.

4. Joule Heating Analysis

4.1. Methodology

Estimation of the Joule heating over the region requires at least the two-dimensional ion and neutral velocities for use in Equation 1. We use a technique similar to L-shell fitting (Ruohoniemi et al., 1989; Villain et al., 1987) which has been used for other mid-latitude ion studies (Clausen et al., 2012; Kunduri et al., 2018; Maimaiti et al., 2018, 2019), whereby the ion motion is assumed to be constant across some area. If such a flow is observed by a SuperDARN radar then the line of sight velocities vary azimuthally across the beams such that if a beam crosses the flow perpendicular to the flow direction it will return with a zero velocity. Conversely, if the beam is sounding in the direction parallel/anti-parallel to the full flow then it will return its full velocity. We can fit a cosine curve to the line of sight velocities against beam azimuth, where the magnitude of the fit provides the full 2D ion flow perpendicular to the magnetic field.

Initially a pre-defined area around the FPI was used where velocities in that area were selected and fit to a cosine curve, however this resulted in poor fits as it became apparent that there were multiple flow patches within the FPI region. Therefore, in order to accurately capture the dynamic ion motion over the FPI, we manually identified the individual ionospheric scatter patches, first by time-integrating the scans over periods of 10 min to reduce temporal variability and then by marking the boundaries of each patch spatially and temporally. We then selected the highest magnitude velocity from each beam within each defined patch and fit to those points. A minimum of five unique beams were used to constrain the fits, which although is less than used in other studies, for example, Thomas and Shepherd (2018); Kunduri et al. (2018), manual (rather than automated) selection and review of the points ensures that they are still constrained to the fit. This further allowed deselecting beams at the sides of patches if by inspecting the fits it became clear that part of the flow does not belong to the patch, ensuring that motion only belonging to that patch was captured.

Figure 6 shows an example of this fitting technique for the BKS scan from 05:51 to 06:01 UT. The top panel shows the scan of line of sight ion velocities plotted onto a geographic grid with the ion velocities corresponding to the colorbar to the right. Positive velocities indicate motion toward the radar, negative velocities away. Non-F-region ionospheric scatter or groundscatter identified by the Ribeiro algorithm has been colored gray. The location of the FPI is plotted at approximately 42° north, 84° west by the orange triangle. The assumed location of the peak neutral wind measurements are shown by the orange dots. The orange boxes mark what has been determined to be a patch of fast moving ionospheric scatter. Since we take the maximum velocity of each beam within a patch, it is only necessary to ensure that the highest velocity within a beam is included within the patch boundaries rather than needing to determine the exact spatial structure of the patch across all radar range gates. At the top right corner of each patch outline, a letter identifier (A, B, C, D and E) has been used to track each patch. At the time of the plot only patches C and D are present. Patches A and B occurred before 05:51 UT, while E after 06:01 UT and so are not shown here. The two panels below show the highest line of sight ion velocities in each beam for both the patches outlined (C) and (D), plotted against their beam azimuths and the resulting cosine fits for each of those cells. A beam azimuth of 0° would point directly to magnetic north, negative azimuths indicate a westwards direction and positive eastwards. If we investigate the points used for fitting, patch C shows velocities that trend to positive at +90° azimuth, while patch D shows velocities that trend to a negative at +90° azimuth. Furthermore Patch C's eastmost beam and patch D's westmost beam show a difference of $\sim$150 ms^{-1} within an azimuth range of only 10–15°. If both of these were included in the same fit, as would occur with a static fitting area, we would be unable to accurately fit it to a sinusoid. This analysis shows that points contained within C and D are therefore part of two separate patches of scatter. Therefore, by including the velocity-azimuth points and their fit results in the patch determination process, we ensure that individual patches are accurately tracked.

By taking the fit magnitudes throughout the interval we are able to estimate the two dimensional ion flow during this period. Then by applying Equation 2 with the IGRF magnetic field strength we can calculate the total local Joule heating across this interval. At high-latitudes, the quasi-vertical magnetic field results in the ion drift traveling approximately parallel to the Earth's surface in the same plane as the neutrals. However, since the magnetic field is inclined (69.26° to the horizontal) at this latitude, the ions and neutrals reference planes are instead inclined roughly 20° relative to each other. The BKS radar only measures the ion velocity in the component perpendicular to $\vec{B}$, it is therefore necessary to mention that the derived fitted velocities may not be the representative of the full three dimensional ion velocities, but only the two dimensional velocities perpendicular to the magnetic field inclination. Due to the magnetic field inclination, it is also important that calculations of the coupling between the ions and neutrals are made in the same plane relative to each other. As there is no estimate of the ion velocity in the direction parallel to the magnetic field, it is not possible to calculate the ion velocity in the plane horizontal to the Earth's surface. Since the FPI observes the geographic horizontal and vertical directions, the neutral wind velocity is obtainable fully in three-dimensions. By applying the three-dimensional rotation matrix transformation given by Equation 3,

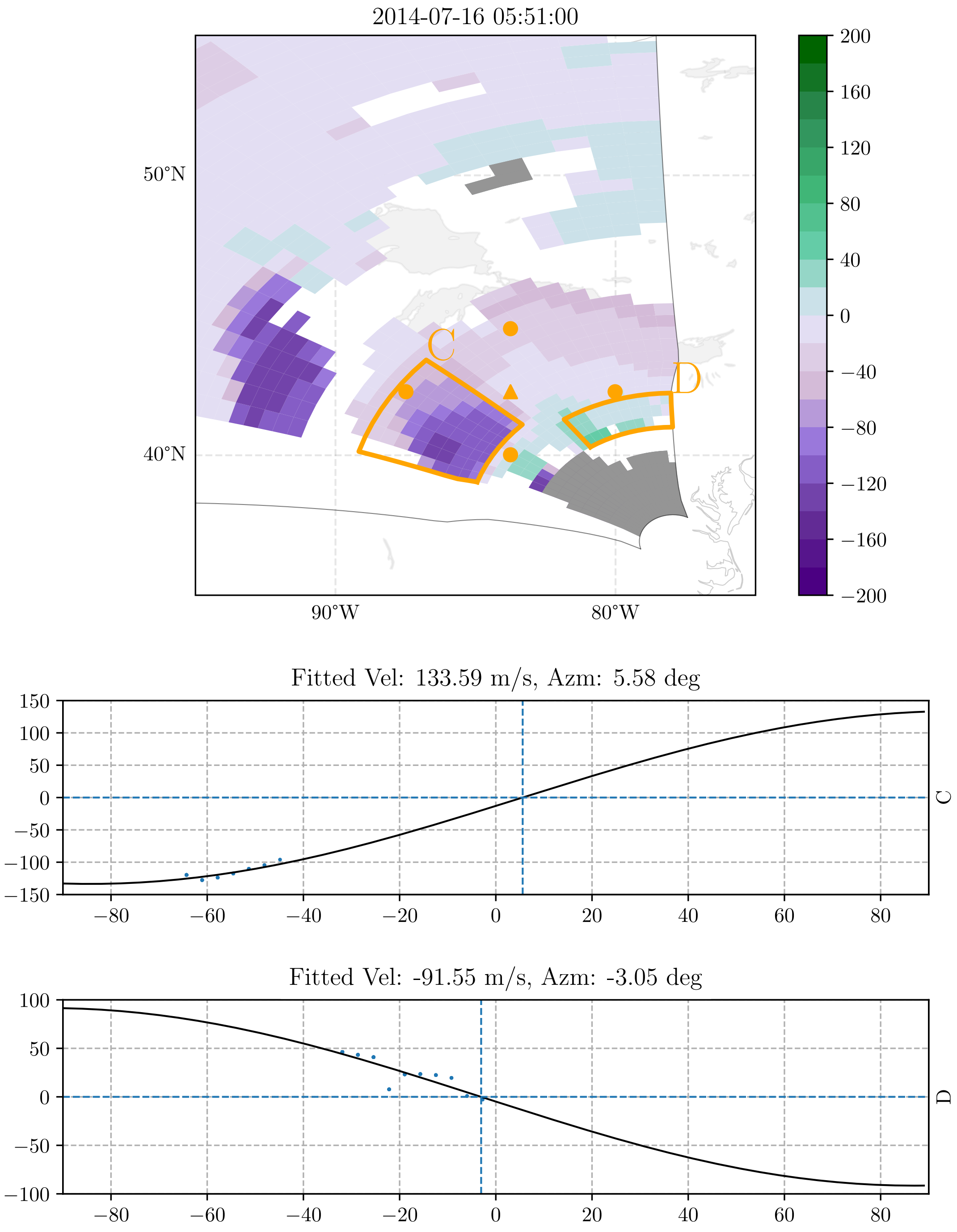

Figure 6. Example 10-minutely integrated scan starting from 05:51 UT of the BKS radar on 16 July 2014, plotted on a geographic map in the top panel. Ion velocities are color coded according to the colorbar on the right, where positive velocities indicate motion toward the radar and negative away. Non-ionospheric scatter as marked by the Ribeiro algorithm is colored gray. The orange triangle represents the location of the ANN FPI, and the orange dots mark the assumed peak neutral wind measurement locations. Outlined in orange with labels are patches identified as C and D. Patches A, B, E are not present at the time of the plot. Below shows the line of sight ion velocities plotted as blue dots against their beam azimuth for each patch outlined in orange and marked with the letter label. The black line represents the least-squares sinusoidal fit where the magnitude of the fit, and azimuth where the fit returns zero is given above each plotting box.

$$\begin{bmatrix} N_{Bz} \\ N_{Bx} \\ N_{By} \end{bmatrix} = \begin{bmatrix} N_{mer} \\ N_{zon} \\ N_{ver} \end{bmatrix} \begin{bmatrix} \cos(\theta) & -\sin(\theta) & 0 \\ \sin(\theta) & \cos(\theta) & 0 \\ 0 & 0 & 1 \end{bmatrix} \begin{bmatrix} \cos(\phi) & 0 & \sin(\phi) \\ 0 & 1 & 0 \\ -\sin(\phi) & 0 & \cos(\phi) \end{bmatrix} \tag{3}$$

where N_{Bz}, N_{Bx}, and N_{By} are the neutral wind components in the z, x, and y directions in magnetic field aligned coordinates respectively, and assuming the magnetic field is entirely in the z direction. N_{mer}, N_{zon}, and N_{ver} are the geographic meridional, zonal and vertical neutral wind components, θ is the angle subtended by the great circle lines connecting the FPI location to the geographic and magnetic north pole, while ϕ is the angle subtended between the magnetic field and the plane horizontal to Earth's surface at the location of the FPI.

As the observed neutral velocities are in the line of sight direction (45° inclination) of the FPI, we calculate the horizontal components of each cardinal observation, W_h, using Equation 4 (Makela et al., 2012),

$$W_h = \frac{W_{LOS} - W_v \sin(\alpha)}{\cos(\alpha)} \tag{4}$$

where W_{LOS} is the line-of-sight Doppler velocity, W_v is the vertical neutral velocity and α is the elevation angle of the line of sight measurements. We assume that the zenith velocity measured above the FPI is consistent across the cardinal locations and so use that as the vertical velocity. The signs of the velocities are then changed such that positive velocities are directed northwards (meridionally) and eastwards (zonally). Because the FPI observations are made at different times with irregular cadences for each cardinal location, we linearly interpolate the observations so that the cadence of opposing north/south and east/west observations match. If only one opposing cardinal measurement is available at a given time, such as after 0600 UT where no southwards observations were taken, we use the measurement we do have as the full meridional/zonal flow.

4.2. Results

Figure 7 shows IMF Bz (a) followed by the estimated observed (blue) and modeled (orange) magnitude of the full neutral wind vector (b). Figure 7c shows the fitted two dimensional ion velocities for each identified patch compared with those modeled by TIEGCM, while (d) shows the Pedersen conductivity, σ_p at the FPI location as modeled by TIEGCM and used for calculating the Joule heating. The solid lines represent the magnitude of the fitted velocity while the shaded region is the RMSE error of the fits. The largest RMSE is less than 20 ms^{-1}, which given that the two major patches (B and C) are always at least 100 ms^{-1} indicates that the fits to determine the two dimensional ion velocities are excellent. The time boundaries for the plot have been restricted to between 04:00 and 08:00 UT since no significant ion patches were identified either side of these times. The observed neutral's speed is seen to steadily increase from ~40 to ~200 ms^{-1} over the course of the night. TIEGCM overestimates the neutral velocities prior to 06:00 UT, however afterward, the total velocity magnitude is in line with the observations. Of the identified ion patches, two take precedence, patches B and C. Patch B appears at 04:00 UT with velocities of 100 ms^{-1}, increasing to in excess of 250 ms^{-1} at 05:00 UT before dissipating. Patch C starts at 05:00 UT, hovering at between 100 and 200 ms^{-1} until it also dissipates at 07:00 UT. It is worth noting that the patches were only marked if they were at least covering part of the region within the FPI measurement locations. It is likely that the patches originated or dissipated outside of this area and merely traversed through the region over the FPI, we have only noted the times where the patch is contained within the FPI region. Furthermore, patch A was identified to occur between 03:50 and 04:20 UT, however the azimuthal span of the patch was not enough to satisfy the conditions we set in Section 3 to fit a two-dimensional velocity, hence it is missing in this and further presentations of the patch ion velocities and Joule heating. TIEGCM's ion velocities remain a fairly steady 20–40 ms^{-1} throughout the interval. As TIEGCM is a global large-scale model, it lacks the micro/mesoscale physics to capture the ion irregularities that produce the ion drift patches observed by the BKS radar, as evidenced here. The Pedersen conductivity is modeled to be relatively constant, although decreasing throughout the nighttime period.

Using the estimated two dimensional ion and neutral velocities, we have calculated the Joule heating rate and its components for each patch, assuming an altitude of 250 km, plotted in Figure 8. Panels a, b, c, d and e show the Joule heating rate and components for patches A, B, C, D, and E respectively. The blue line represents the ion

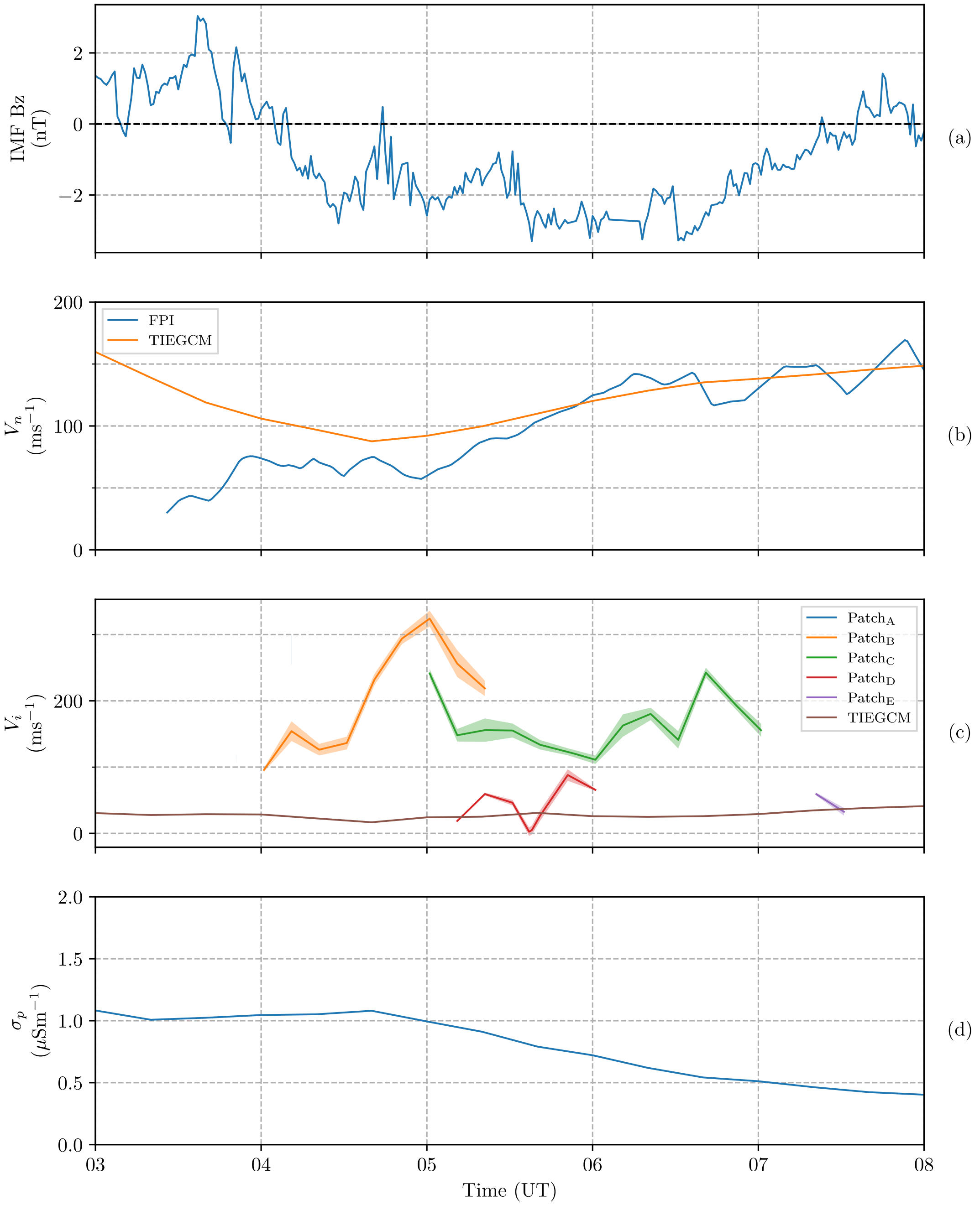

Figure 7. (a) IMF Bz followed by, (b) the magnitude of the full neutral wind vector in blue with TIEGCM's neutral velocities in orange, (c) the magnitude of the full ion velocities for each identified patch. The dark lines represent the fitted values, the shaded region either side of the line shows the root mean squared error (RMSE) of the fit used to estimate the velocity. The TIEGCM ion velocities are plotted as the burgundy line without a RMSE shaded region. (d) Shows the Pedersen conductivity at the FPI location, as modeled by TIEGCM.

heating rate, Q_i, the orange and green lines the two wind correction terms, Q_{w1} and Q_{w2} respectively and the red line the total Joule heating rate of the patch, calculated as the sum of the three components. A negative Q_{w1} indicates that the direction of the ion and neutrals were aligned with each other, resulting in fewer collisional interactions and thus dampening the overall heating rate, a positive value indicates the ions and neutrals were opposed. Panel f shows the same components, but as modeled by TIEGCM. The final panel, g, compares the average total Joule heating rate from all the patches over the FPI region, with the total heating rate modeled by

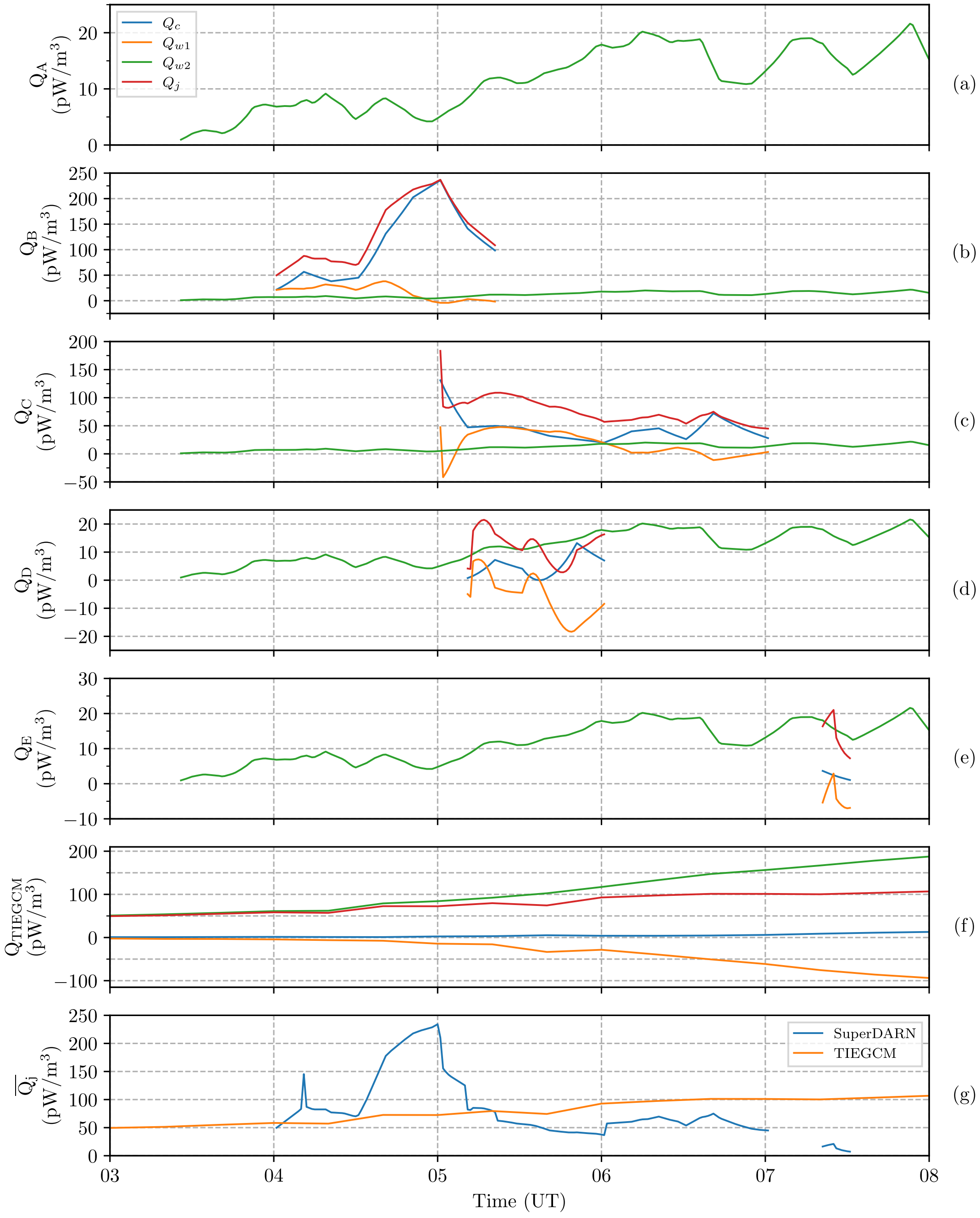

Figure 8. Panels a, b, c, d and e shows the estimated Joule heating components and total heating for each identified patch, the panel labels correspond to the patch velocity labels shown in Figure 7c. Each component is plotted according to the legend in panel a. Panel f shows the Joule heating components and total heating modeled by TIEGCM. g shows the total Joule heating rate calculated as the average heating rate of all patches in the common area, while re-plotting TIEGCM's total Joule heating in orange for comparison.

TIEGCM. The TIEGCM Joule heating has been calculated by using its ion and neutral velocities for use in Equation 2, while keeping the other parameters the same as the observations, therefore the only difference between the observed and modeled Joule heating rates, are the observed and modeled ion/neutral velocities. Based on the measurements, the most significant heating rate occurred between 04:30 and 05:00 UT which resulted from ion motion from patch B, with heating due to ion motion, Q_i, peaking at roughly 236 pWm^{-3} out of its total heating, Q_j, of 237 pWm^{-3}. Patch C also exhibited some enhanced ion heating at 49.1 pWm^{-3}, however this is somewhat lower than the severe excitations in patch B.

The positive magnitude of Q_{w1} in patch C and D indicates that the ions and neutrals were opposed in direction for most of each patch and so collisional interactions were increased. This increase is greatest in patch D at ~05:20 UT, where the total heating is increased by 47 pWm^{-3} to 109 pWm^{-3}, resulting in a 78% increase due to the ion-neutral directions. The impact of this term is further shown in patch D, where at ~05:50 UT, Q_{w1} is its most negative value and results in decreasing the total Joule heating by ~76%. The heating directly due to the neutrals Q_{w2} is low throughout the entire interval, hovering at around ~5 pWm^{-3}, therefore despite the large influence of the neutral wind direction on the total heating rate, the overall Joule heating magnitude is only significantly enhanced by ion motion.

The Joule heating enhancement observed in panel g at 05:00 UT that peaked with a magnitude of 235 pWm^{-3} is nearly 8 times higher than the TIEGCM modeled Joule heating of 30.8 pWm^{-3}. Aside from ±20 min of the 05:00 UT peak, the TIEGCM Joule heating rate is significantly higher than the observational estimate. When we investigate the reason behind the heating we find that the larger magnitudes in the observed ion heating, Q_i, especially in patch C, indicates that the observed heating is due to ion motion. Panel f shows that the magnitude of the total heating in TIEGCM is due to faster motion of the neutral winds, Q_{w2}, whose significance increases throughout the interval compared to the ion contribution. During this event, we find that our observations disagree with not just the magnitude of the modeled Joule heating rate at the mid-latitudes, but the modeled Joule heating being from greater neutral wind motion disagrees with that calculated from our observations.

5. Discussion

The strong westwards driven ion flows that are observed in Figure 3 which persist through a longitude range of approximately 30° from 80°W to 110°W, could indicate that the flows captured in the FPI region are part of a SAPS. SAPS do not typically occur during low geomagnetic activities, however Kunduri et al. (2017) found SAPS to occur 15% of the time in the nightside during relatively quiet conditions with velocities ~100 ms^{-1} (Kunduri et al., 2018). Kunduri et al. (2021) also found SAPS latitudinal distribution to correlate strongly with the ionospheric trough, which during this interval lies poleward of the FPI, suggesting that it would be unlikely for the flows to be a SAPS. Confirmation of the ion flows (not) being part of SAPS would require ion flux measurements from satellite observations (Clausen et al., 2012; Grocott et al., 2011; Kunduri et al., 2017, 2018), however coincidental measurements were not available for the interval of this study. Instead we compare with findings from Kunduri et al. (2017), which studied the latitudinal distribution of SAPS with correlation to the DST index. At 0600 UT (0030 MLT at the FPI location) the DST index was −1, which according to Kunduri et al. (2017), would place the mean SAPS position at 61° magnetic latitude (~51° geographic) with a minimum of 59° magnetic latitude (~49° geographic), which would still be at least 7° poleward of the FPI location. Furthermore Nagano et al. (2015) calculated a quantitative estimation of the lower latitudinal boundary for SAPS keyed by SYM-H, which during this interval reached a minimum of −20 nT. According to Nagano et al. (2015) this would result in a lower latitude boundary for SAPS of ~58° magnetic latitude (~48° geographic), still poleward of the FPI. We therefore suggest that the observations during this interval are not likely due to SAPS. If the ion enhancements are not due to high-latitude convection or to a SAPS, they may instead be part of a persistent quiet-time mid-latitude nighttime feature (Clausen et al., 2012; Greenwald et al., 2006) that appears due to pressure gradient instabilities often found at the equatorward boundary of the ionospheric trough (Greenwald et al., 2006; Hudson & Kelley, 1976; Liu et al., 2021), which would align spatially with our observations. While we suggest the ions to be primarily responsible for the increased Joule heating rates, we might expect currents to be present in the region of those Joule heating enhancements. However, there is no evidence of field-aligned currents at the FPI location, which is concerning and could be investigated further in future works. We do provide one possible explanation for the lack of FAC's in the region, which could be due to ions and electrons flowing in the same direction at 250 km altitude, potentially preventing any current from being produced.

Previous studies investigating mid-latitude nighttime ionospheric scatter have found ion velocities typically less than 100 ms^{-1} (Greenwald et al., 2006; Maimaiti et al., 2018, 2019). They are often attributed to penetrating electric fields, driven by the neutral wind dynamo or due to pressure gradient forces. Given the magnitude of Q_{w2} is small compared to the total Joule heating rate, Q_j, in this study, we infer that the ions are responsible for driving the increased Joule heating rate. Maimaiti et al. (2018, 2019) carried out statistical studies of the nightside mid-latitude and sub-auroral ionospheric convection and found persistent westward flows between 20 and 90 ms^{-1} depending on season and MLT, which is somewhat slower than our results, particularly as they found that the fastest flows occurred in winter. Although Maimaiti et al. (2018) used the same groundscatter algorithm (Ribeiro et al., 2011) as in this study to remove low velocity non-ionospheric scatter, they also deployed the additional technique as described in Ribeiro et al. (2012), where events were only considered if the 3rd and 97th percentile of their ion velocity distributions were greater than -120 ms^{-1} and less than 120 ms^{-1} respectively. This ensured that they only studied the quiet time mid-latitude nighttime scatter, however rare fast events may have been lost. By selecting active patches in this study, we have not considered low-velocity ionospheric scatter during this event, this will have skewed our velocities to a higher range than theirs. We believe that the higher ion velocities estimated in this study are therefore reasonable. Furthermore, despite our ion velocities being greater than other quiet time studies, they are significantly slower than other mid-latitude studies that occur under geomagnetically active periods. When enhanced ion velocities have been observed due to the equatorward expansion of auroral convection (Joshi et al., 2015) or SAPS (Billett et al., 2022; Clausen et al., 2012) velocities are observed in excess of 500 ms^{-1} and up to 1,000 ms^{-1}. Our observed ion velocities therefore fall within a reasonable expectation when considering the geomagnetic activity and methods used in this study.

Strong ion motion has been shown to drive the neutral atmosphere into a similar direction as momentum is exchanged through frictional collisions. During both patches C and D the directions of the ions and neutrals are initially opposed, resulting in an increased Joule heating rate, however as both patches persist, the neutrals are slowly driven into the same direction as the ions, given by Q_{w1} decreasing. When the ion driving to the neutrals is at its greatest Q_{w1} would reach its peak negative value, and start to increase once the ion driving recedes and the neutrals retain momentum and start to drive the ions. In our observations Q_{w1} continues to decrease and never reach a negative peak over the tracked lifespan of both patches, with patch B lasting ~1.5 hr and patch C ~2 hr, suggesting the ions continue to drive the neutral motion throughout the period where we track them. Joshi et al. (2015) calculated the mid-latitude ion neutral coupling timescale during a geomagnetic storm and found a time-lag of ~84 min for the neutrals to respond to the ion driving. Billett et al. (2022) found a response time of 2 hr for mid-latitude neutral wind to respond to pressure gradient forces. In the case of Joshi et al. (2015), ions were driven by expanded auroral convection during a geomagnetic storm, and for Billett et al. (2022) a SAPS event, with ion velocities several 100 ms^{-1} faster than this study's quiet time events. Kosch et al. (2001) found an average of high-latitude response times during geomagnetically quiet periods to be 3.3 hr. While we cannot calculate the full neutral coupling timescale because the neutrals never reach a steady state with the ions, the timescales in our observations can be viewed as the minimum value for the coupling timescale. Our values are close to the full values from Joshi et al. (2015) and Billett et al. (2022), but are still smaller than those from the high-latitude timescales from Kosch et al. (2001), indicating that our values are reasonable.

Studies by Aruliah et al. (2005) and C. Anderson et al. (2013) investigated the impact that neutral winds have on Joule heating rate estimations. They calculated the high-latitude neutral wind dynamo to account for 29% (Aruliah et al., 2005) and 36% (C. Anderson et al., 2013) of the total Joule heating rates. Across patches B, C and D, the average neutral contribution (Q_w) to the total heating rate was 24.7%, 40.4%, and 43.1% respectively, which is consistent with the previous studies, albeit at different latitudes. Patch B's lower neutral contribution can be accounted for by the significantly stronger ion enhancements than in the other two patches, while their contributions although higher, still signify the majority of mid-latitude Joule heating response being due to the ions. Billett et al. (2018) indicated that the high-latitude Joule heating rate was nearly entirely eliminated when the neutral wind was pulled into the orientation of the ion flow. Kiene et al. (2019) used a scanning doppler imager with a SuperDARN radar to estimate high-latitude local Joule heating rates. They found that inclusion of the neutral winds in their Joule heating rate calculations dropped the total heating rate by a factor of ≃3 at high-latitudes. At the minimum value of Q_{w1}, which occurred in patch D, the Joule heating rate was decreased from 24.1 pWm^{-3} to 5.61 pWm^{-3}, representing a 4.2 times decrease, similar to the observations found in Kiene et al. (2019). However, our observations vary substantially with the winds either contributing positively or negatively to the total heating rate, amounting to either a $>|75\%|$ increase or reduction in the total Joule heating rate depending on the neutral flow direction relative to the ions. When considering the multiplicative reduction, and the percentage decreases, our results show that the neutral winds have a significant reducing action on the overall Joule heating rate in line with the results obtained by the high-latitude studies of Billett et al. (2018); Kiene et al. (2019). Although these studies did not show cases of the neutrals increasing the heating, Aruliah et al. (2005) and C. Anderson et al. (2013) did find that high-latitude neutrals were able to enhance or reduce the total Joule heating rates as similarly shown in this study. The increased heating rate magnitude of ∼75% in this study is symmetrical to the heating magnitude when the neutrals were decreasing the heating rate, implying that the neutrals are equally effective at enhancing Joule heating rates as they are at dampening them.

Typically, studies investigating Joule heating rates calculate a height-integrated value using model values (McHarg et al., 2005; Lu et al., 2016; X. X. Zhang et al., 2005) or based on assumptions of the height integrated neutral pattern being representative of the neutral pattern at approximately 160 km altitude (Billett et al., 2018) as shown by Lu et al. (1995), or by assuming that F-region altitude measurements map down to a range of altitudes (Cai et al., 2014). Direct comparisons of our values to other studies are somewhat limited, however C. Anderson et al. (2013) and Kiene et al. (2019) calculated high-resolution high-latitude local Joule-heating rates using instruments observing the ions and neutrals at 250 km, which provides an excellent comparison to our mid-latitude study. The Joule heating rate in this study peaks at ∼235 $\mathrm{pWm^{-3}}$. Both C. Anderson et al. (2013) and Kiene et al. (2019) estimated the local high-latitude Joule heating rates up to the order of $\mathrm{nWm^{-3}}$ for geomagnetically active intervals, an order of magnitude higher than our observations. The majority of their observations however were in the tens, or hundreds of $\mathrm{pWm^{-3}}$, which matches our observations, suggesting small patches of ion scatter at mid-latitudes are able to produce local Joule heating enhancements similar to those observed at high-latitudes. Their most dominant Joule heating values were coincident with the auroral region, where ion velocities are typically much higher, often in excess of 1,000 $\mathrm{ms^{-2}}$, particularly during geomagnetically intense periods (such as in their studies). While we could compare our values with studies calculating height-integrated Joule heating rates by assuming that the electric field maps to lower altitudes, the neutral wind measurements however do not, and doing so would introduce significant uncertainty into our calculations that we have attempted to avoid by keeping the ion and neutral measurements as co-located as possible. Nevertheless, they can be used as an insight into the difference between auroral and sub-auroral Joule heating rates, which typically indicate higher magnitudes in the auroral region, with the difference of at least an order of magnitude being fairly common (Billett et al., 2018; Lu et al., 2016; X. X. Zhang et al., 2005). Our values being an order of magnitude smaller than those in the high-latitude studies is reasonable. If we consider the fact that the high-latitude studies occurred during geomagnetically intense periods, while our mid-latitude study is during a quiet time period, our Joule heating values may be closer than expected, indicating that even small transient events can result in a significant Joule heating deposition in the mid-latitudes.

Baloukidis et al. (2023) compared statistical high-latitude Joule heating distributions estimated by using the European incoherent scatter scientific association (EISCAT) radars with TIEGCM. Their EISCAT Joule heating estimations ranged from altitudes of 80–150 km altitude and did not include the neutral wind contributions, so are not directly comparable to our estimations in this study, but their comparisons to TIEGCM are still useful. They found that during low Kp, TIEGCM's modeled Joule heating was higher than their observed estimates. If we can assume that fast moving ion patches were averaged out in their low Kp statistical analysis, then our results of TIEGCM modeling higher Joule heating during low velocity ion events agrees with the findings from their study. At higher Kp, Baloukidis et al. (2023) also found TIEGCM's observed Joule heating was lower than their observed estimates. Although our study is a low Kp event, our periods of significant ion enhancements are more often associated with high levels of geomagnetic activity, so we can compare our fast moving ion patches to their high Kp analysis, whereby we also agree that TIEGCM's modeled Joule heating is lower than observed estimations. Similar to our findings, Baloukidis et al. (2023) remark that the difference in their discrepancies between TIEGCM and their observations are due to small-scale effects that amount to sub-grid variability within TIEGCM that it cannot resolve. Due to this sub-grid variability, TIEGCM includes an empirically-derived multiplication factor named JOULEFAC to increase its internal Joule heating by a fixed factor of 1.5 (NCAR, 2016) in order for its neutral temperatures to better agree with statistical observations. One solution Baloukidis et al. (2023) propose is to adjust JOULEFAC with Kp so that different values are used for different levels of geomagnetic activity. Previous studies have manually adjusted the value of JOULEFAC to better reproduce realistic Joule heating values (Emery et al., 1999). Although there may be differences between optimized JOULEFAC values for high and mid-latitudes, optimized JOULEFAC values may work on a statistical level, however it could not account for small scale spatial or temporal events such as in this study. A better JOULEFAC for low Kp may bring TIEGCM's modeled Joule heating in line with our observed estimations for low velocity patches, however there would still be a large and potentially greater difference for excited ion motion, such as patch B between 04:30 and 05:00 UT in this study. Furthermore, adjusting JOULEFAC may "correct" the numerical Joule heating value, however it might not solve discrepancies between whether greater ion or neutral motion produces Joule heating as occurs in this study. Rather, if focusing on localized studies, improvements should be made for TIEGCM to better model the microscale electrodynamics of the mid-latitude ionosphere.

6. Conclusion

During the night of 16 July 2014 over mid-latitude North America the BKS SuperDARN radar observed highly localized ion velocity enhancements of over 200 ms^{-1} while ANN FPI observed neutral velocities over 150 ms^{-1} despite the lack of strong geomagnetic drivers. The use of combined AMPERE and TEC data sets shows the ion enhancements are sub-auroral, and likely driven by plasma gradient instabilities, a common quiet-time nighttime mid-latitude occurrence observed at the equatorward edge of the mid-latitude trough. The ion velocity increases drove significant Joule heating enhancements to the region, of a similar magnitude to results from high-latitude studies, with the maximum increases only a single order of magnitude less than under high-latitude geomagnetically active periods. The neutral wind was shown to have a significant impact on the overall heating rate, accounting for on average between 24% and 43% of the total heating, while at the extremes increasing or decreasing the total heating rate by in excess of 75%.

Comparisons with modeled ion and neutral velocities from TIEGCM indicate that TIEGCM does not model equivalent enhancements to the ion velocities due to being a large-scale model that does not include microscale electrodynamical processes, resulting in an approximate 8 times smaller modeled Joule heating rate than during the peak observed estimates. Although TIEGCM does a good job of modeling the meridional neutral velocities, the zonal velocities were an order of magnitude higher than our observations, enough to amplify the total neutral wind velocity such that the mid-latitude Joule heating reported by the model was due to greater motion of the neutrals rather than the ions as our observations suggest. The strong neutral wind in the model also resulted in a greater modeled Joule heating rate than our observational estimates during quieter periods of the interval.

Opportunities for studying mid-latitude ion-neutral coupling and the Joule heating response are rare and limited intervals exist with measurements from coincident instruments, particularly during quiet times to study such events, nevertheless further work is needed to better understand the dynamics of the mid-latitude ionosphere-thermosphere, especially during non-geomagnetically intense periods. Further understanding and better representation of the mid-latitude dynamics could help produce more accurate models for Joule heating predictions.

Data Availability Statement

All data used for this study are available from open-source nonprofit organisations. The authors acknowledge the use of SuperDARN data. SuperDARN is a collection of radars funded by national scientific funding agencies of Australia, Canada, China, France, Italy, Japan, Norway, South Africa, United Kingdom, and United States of America, and we thank the international PI team for providing the data. The authors acknowledge access to the SuperDARN database via the British Antarctic Survey (https://www.bas.ac.uk/project/superdarn/data). Other data mirrors are hosted by the Virginia Tech SuperDARN group (http://vt.superdarn.org/) and the University of Saskatchewan (https://superdarn.ca/data-download). The radar data products used are the FITACF3.0 library and version 5.0 of the Radar Software Toolkit (RST) (Thomas et al., 2022). The authors acknowledge use of NATION data, operated through support from the National Science Foundation and collaboration between the University of Illinois, the University of Michigan, Clemson University, Eastern Kentucky University, the Psigah Astronomical Research Institute, and Virginia Tech, NATION data can be found at the Madrigal Millstone Hill data repository (http://millstonehill.haystack.mit.edu/index.html). We thank the AMPERE team and the AMPERE Science Data Center for providing data products derived from the Iridium Communications constellation, enabled by support from the National Science Foundation, AMPERE data was obtained from https://ampere.jhuapl.edu/browse/. Data for TEC processing are provided from the following organizations: UNAVCO, Scripps Orbit and Permanent Array Center, Institut Geographique National, France, International GNSS Service, The Crustal Dynamics Data Information System (CDDIS), National Geodetic Survey, Instituto Brasileiro de Geografia e Estatística, RAMSAC CORS of Instituto Geográfico Nacional de la República Argentina, Arecibo Observatory, Low-Latitude Ionospheric Sensor Network (LISN), Topcon Positioning Systems, Inc., Canadian High Arctic Ionospheric Network, Centro di Ricerche Sismologiche, Système d'Ob-servation du Niveau des Eaux Littorales (SONEL), RENAG: REseau NAtional GPS permanent, GeoNet the official source of geological hazard information for New Zealand, GNSS Reference Networks, Finnish Meteorological Institute, and SWEPOS Sweden. Access to these data are provided by madrigal network via: http://cedar.openmadrigal.org/. Data analysis and visualisations in this paper were generated using the free open-source software packages aacgmv2 v2.6.2 (Shepherd, 2014; A. Burrell et al., 2020) and pyDarn version 3.1.1 (Martin et al., 2023). All solar wind data and geomagnetic indices were downloaded from NASA's SPDF Coordinated Data Analysis Web (https://cdaweb.gsfc.nasa.gov/index.html/). The AE data are also available from the WDC for Geomagnetism, Kyoto (http://wdc.kugi.kyoto-u.ac.jp/wdc/Sec3.html) who prepared this index. The Kp index data resources are available at https://www.gfz-potsdam.de/en/kp-index/.

Acknowledgments

EKD acknowledges funding by the NERC doctoral grant NE/S007423/1. MTW and AG were funded by the UKRI NERC project NE/T000937/1. AG was funded by UKRI NERC projects NE/W003090/1 and NE/W003015/1. MTW was funded by UKRI STFC Ernest Rutherford Fellowship project ST/X003663/1. GL was supported in part by NASA LWS Program under award 80NSSC20K1784 and by NASA HSR Program under award 80NSSC21K1673. The National Center for Atmospheric Research is a major facility sponsored by the National Science Foundation under Cooperative Agreement No. 1852977. The authors would like to thank the National Science Foundation for awards AGS-6943256 and the Office of Naval research for award N00014-23-1-2160. We would like to thank J. J. Makela for providing NATION data and for useful discussions on its use. The Blackstone SuperDARN radar is maintained and operated by Virginia Tech under support by NSF Grant AGS-1935110. TEC data is provided to the community by the Massachusetts Institute of Technology (MIT) under support from US National Science Foundation Grant AGS-1952737. We gratefully acknowledge the use of The High End Computing facility at Lancaster University which has facilitated the necessary data processing for this study. TIEGCM simulation results have been provided by the Community Coordinated Modeling Center (CCMC) at Goddard Space Flight Center through their publicly available simulation services (https://ccmc.gsfc.nasa.gov).

References

Alken, P., Thébault, E., Beggan, C. D., Amit, H., Aubert, J., Baerenzung, J., et al. (2021). International geomagnetic reference field: The thirteenth generation. *Earth Planets and Space*, *73*(1), 49. https://doi.org/10.1186/s40623-020-01288-x

Anderson, B. J., Takahashi, K., & Toth, B. A. (2000). Sensing global Baekeland currents with iridium engineering magnetometer data. *Geophysical Research Letters*, *27*(24), 4045–4048. https://doi.org/10.1029/2000GL000094

Anderson, C., Kosch, M. J., Nicolls, M. J., & Conde, M. (2013). Ion-neutral coupling in earth's thermosphere, estimated from concurrent radar and optical observations above Alaska. *Journal of Atmospheric and Solar-Terrestrial Physics*, *105–106*, 313–324. https://doi.org/10.1016/j.jastp.2013.04.005

Anderson, P. C., Hanson, W. B., Heelis, R. A., Craven, J. D., Baker, D. N., & Frank, L. A. (1993). A proposed production model of rapid subauroral ion drifts and their relationship to substorm evolution. *Journal of Geophysical Research*, *98*(A4), 6069–6078. https://doi.org/10.1029/92ja01975

Aruliah, A. L., Griffin, E. M., Aylward, A. D., Ford, E. A. K., Kosch, M. J., Davis, C. J., et al. (2005). First direct evidence of meso-scale variability on ion-neutral dynamics using co-located tristatic FPIS and EISCAT radar in northern Scandinavia. *Annales Geophysicae*, *23*(1), 147–162. https://doi.org/10.5194/angeo-23-147-2005

Baker, J. B., Zhang, Y., Greenwald, R. A., Paxton, L. J., & Morrison, D. (2004). Height-integrated joule and auroral particle heating in the night side high latitude thermosphere. *Geophysical Research Letters*, *31*(9). https://doi.org/10.1029/2004GL019535

Baloukidis, D., Sarris, T., Tourgaidis, S., Pirnaris, P., Aikio, A., Virtanen, I., et al. (2023). A comparative assessment of the distribution of joule heating in altitude as estimated in tie-GCM and EISCAT over one solar cycle. *Journal of Geophysical Research: Space Physics*, *128*(12), e2023JA031526. https://doi.org/10.1029/2023JA031526

Billett, D. D., Grocott, A., Wild, J. A., Walach, M. T., & Kosch, M. J. (2018). Diurnal variations in global joule heating morphology and magnitude due to neutral winds. *Journal of Geophysical Research: Space Physics*, *123*(3), 2398–2411. https://doi.org/10.1002/2017JA025141

Billett, D. D., Mcwilliams, K. A., Kerr, R. B., Makela, J. J., Chartier, A. T., Ruohoniemi, J. M., et al. (2022). Mid-latitude neutral wind responses to sub-auroral polarization streams. *Annales Geophysicae*, *40*(5), 571–583. https://doi.org/10.5194/angeo-40-571-2022

Burrell, A., van der Meeren, C., & Laundal, K. M. (2020). aacgmv2 [Software]. *Zenodo*. https://zenodo.org/doi/10.5281/zenodo.1212694

Burrell, A. G., Perry, G. W., Yeoman, T. K., Milan, S. E., & Stoneback, R. (2018). Solar influences on the return direction of high-frequency radar backscatter. *Radio Science*, *53*(4), 577–597. https://doi.org/10.1002/2017RS006512

Cai, L., Aikio, A. T., & Nygrén, T. (2014). Solar wind effect on joule heating in the high-latitude ionosphere. *Journal of Geophysical Research: Space Physics*, *119*(12), 10440–10455. https://doi.org/10.1002/2014JA020269

Chisham, G., Lester, M., Milan, S. E., Freeman, M. P., Bristow, W. A., Grocott, A., et al. (2007). A decade of the super dual auroral radar network (superDARN): Scientific achievements, new techniques and future directions. *Surveys in Geophysics*, *28*(1), 33–109. https://doi.org/10.1007/s10712-007-9017-8

Clausen, L. B., Baker, J. B., Ruohoniemi, J. M., Greenwald, R. A., Thomas, E. G., Shepherd, S. G., et al. (2012). Large-scale observations of a subauroral polarization stream by midlatitude superdarn radars: Instantaneous longitudinal velocity variations. *Journal of Geophysical Research*, *117*(A5), A05306. https://doi.org/10.1029/2011JA017232

Cowley, S. W. H., & Lockwood, M. (1992). Excitation and decay of solar wind-driven flows in the magnetosphere-ionosphere system. *Copernicus*, *10*, 103–115.

Coxon, J. C., Milan, S. E., & Anderson, B. J. (2018). *A review of Baekeland current research using ampere* (pp. 257–278). American Geophysical Union (AGU). https://doi.org/10.1002/9781119324522.ch16

Dang, T., Li, X., Luo, B., Li, R., Zhang, B., Pham, K., et al. (2022). Unveiling the space weather during the starlink satellites destruction event on 4 February 2022. *Space Weather*, *20*(8), e2022SW003152. https://doi.org/10.1029/2022SW003152

Dungey, J. W. (1961). Interplanetary magnetic field and the auroral zones. *Physical Review Letters*, *6*(2), 47–48. https://doi.org/10.1103/physrevlett.6.47

Emery, B. A., Lathuilere, C., Richards, P. G., Roble, R. G., Buonsanto, J., Knipp, J., et al. (1999). Time dependent thermospheric neutral response TOTHE 2–11 November 1993 storm period. *Journal of Atmospheric and Solar-Terrestrial Physics*, *61*(3–4), 329–350. https://doi.org/10.1016/S1364-6826(98)00137-0

Fang, T., Kubaryk, A., Goldstein, D., Li, Z., Fuller-Rowell, T., Millward, G., et al. (2022). Space weather environment during the spaceX starlink satellite loss in February 2022. *Space Weather*, *20*(11), e2022SW003193. https://doi.org/10.1029/2022SW003193

Fuller-Rowell, T. J., Codrescu, M. V., Roble, R. G., & Richmond, A. D. (1997). How does the thermosphere and ionosphere react to a geomagnetic storm? (pp. 203–225). https://doi.org/10.1029/GM098p0203

Greenwald, R. A., Baker, K. B., Dudeney, J. R., Pinnock, M., Jones, T. B., Thomas, E. C., et al. (1995). Darn/superDARN. *Space Science Reviews*, *71*(1–4), 761–796. https://doi.org/10.1007/bf00751350

Greenwald, R. A., Oksavik, K., Erickson, P. J., Lind, F. D., Ruohoniemi, J. M., Baker, J. B. H., & Gjerloev, J. W. (2006). Identification of the temperature gradient instability as the source of decameter-scale ionospheric irregularities on plasmapause field lines. *Geophysical Research Letters*, *33*(18), L18105. https://doi.org/10.1029/2006GL026581

Grocott, A., Milan, S. E., Baker, J. B., Freeman, M. P., Lester, M., & Yeoman, T. K. (2011). Dynamic subauroral ionospheric electric fields observed by the Falkland Islands radar during the course of a geomagnetic storm. *Journal of Geophysical Research*, *116*(A11), A11202. https://doi.org/10.1029/2011JA016763

Harding, B. J., Gehrels, T. W., & Makela, J. J. (2014). Nonlinear regression method for estimating neutral wind and temperature from Fabry–Perot interferometer data. *Applied Optics*, *53*(4), 666–673. https://doi.org/10.1364/AO.53.000666

Heelis, R. A., Lowell, J. K., & Spiro, R. W. (1982). A model of the high-latitude ionospheric convection pattern. *Journal of Geophysical Research*, *87*(A8), 6339–6345. https://doi.org/10.1029/ja087ia08p06339

Howell, D. C. (2005). *Median absolute deviation*. John Wiley and Sons, Ltd. https://doi.org/10.1002/0470013192.bsa384

Hudson, M. K., & Kelley, M. C. (1976). The temperature gradient drift instability at the equatorward edge of the ionospheric plasma trough. *Journal of Geophysical Research*, *81*(22), 3913–3918. https://doi.org/10.1029/JA081i022p03913

Joshi, P. P., Baker, J. B. H., Ruohoniemi, J. M., Makela, J. J., Fisher, D. J., Harding, B. J., et al. (2015). Observations of storm time midlatitude ion-neutral coupling using superDARN radars and NATION Fabry-Perot interferometers. *Journal of Geophysical Research A: Space Physics*, *120*, 8989–9003. https://doi.org/10.1002/2015JA021475

Knipp, D. J., Tobiska, W. K., & Emery, B. A. (2004). Direct and indirect thermospheric heating sources for solar cycles 21-23 (Vol. *224*).

Kiene, A., Bristow, W. A., Conde, M. G., & Hampton, D. L. (2019). High-resolution local measurements of F region ion temperatures and joule heating rates using superDARN and ground-based optics. *Journal of Geophysical Research: Space Physics*, *124*(1), 557–572. https://doi.org/10.1029/2018JA025997

Kilcommons, L. M., Redmon, R. J., & Knipp, D. J. (2017). A new DMSP magnetometer and auroral boundary data set and estimates of field-aligned currents in dynamic auroral boundary coordinates. *Journal of Geophysical Research: Space Physics*, *122*(8), 9068–9079. https://doi.org/10.1002/2016JA023342

Knipp, D. J., Emery, B. A., Engebretson, M., Li, X., McAllister, A. H., Mukai, T., et al. (1998). An overview of the early November 1993 geomagnetic storm. *Journal of Geophysical Research*, *103*(A11), 26197–26220. https://doi.org/10.1029/98ja00762

Kosch, M. J., Cierpka, K., Rietveld, M. T., Hagfors, T., & Schlegel, K. (2001). High-latitude ground-based observations of the thermosphericion-drag time constant. *Geophysical Research Letters*, *28*(7), 1395–1398. https://doi.org/10.1029/2000GL012380

Kunduri, B. S., Baker, J. B., Ruohoniemi, J. M., Coster, A. J., Vines, S. K., Anderson, B. J., et al. (2021). An examination of magnetosphere-ionosphere influences during a saps event. *Geophysical Research Letters*, *48*(19), e2021GL095751. https://doi.org/10.1029/2021GL095751

Kunduri, B. S., Baker, J. B., Ruohoniemi, J. M., Nishitani, N., Oksavik, K., Erickson, P. J., et al. (2018). A new empirical model of the subauroral polarization stream. *Journal of Geophysical Research: Space Physics*, *123*(9), 7342–7357. https://doi.org/10.1029/2018JA025690

Kunduri, B. S., Baker, J. B., Ruohoniemi, J. M., Thomas, E. G., Shepherd, S. G., & Sterne, K. T. (2017). Statistical characterization of the large-scale structure of the subauroral polarization stream. *Journal of Geophysical Research: Space Physics*, *122*(6), 6035–6048. https://doi.org/10.1002/2017JA024131

Lin, D., Wang, W., Garcia-Sage, K., Yue, J., Merkin, V., McInerney, J. M., et al. (2022). Thermospheric neutral density variation during the "spaceX" storm: Implications from physics-based whole geospace modeling. *Space Weather*, *20*(12), e2022SW003254. https://doi.org/10.1029/2022SW003254

Liu, Y., Xiong, C., Wan, X., Lai, Y., Wang, Y., Yu, X., & Ou, M. (2021). Instability mechanisms for the f-region plasma irregularities inside the midlatitude ionospheric trough: Swarm observations. *Space Weather*, *19*(7), e2021SW002785. https://doi.org/10.1029/2021SW002785

Lu, G., Baker, D. N., McPherron, R. L., Farrugia, C. J., Lummerzheim, D., Ruohoniemi, J. M., et al. (1998). Global energy deposition during the January 1997 magnetic cloud event. *Journal of Geophysical Research*, *103*(A6), 11685–11694. https://doi.org/10.1029/98ja00897

Lu, G., Emery, B. A., Rodger, A. S., Lester, M., Taylor, J. R., Evans, D. S., et al. (1996). High-latitude ionospheric electrodynamics as determined by the assimilative mapping of ionospheric electrodynamics procedure for the conjunctive sundial/atlas 1/gem period of March 28-29, 1992. *Journal of Geophysical Research*, *101*(A12), 26697–26718. https://doi.org/10.1029/96ja00513

Lu, G., Richmond, A. D., Emery, B. A., & Roble, R. G. (1995). Magnetosphere-ionosphere-thermosphere coupling: Effect of neutral winds on energy transfer and field-aligned current. *Journal of Geophysical Research*, *100*(A10), 19643–19659. https://doi.org/10.1029/95ja00766

Lu, G., Richmond, A. D., Lühr, H., & Paxton, L. (2016). High-latitude energy input and its impact on the thermosphere. *Journal of Geophysical Research: Space Physics*, *121*(7), 7108–7124. https://doi.org/10.1002/2015JA022294

Maimaiti, M., Baker, J. B., Ruohoniemi, J. M., & Kunduri, B. (2019). Morphology of nightside subauroral ionospheric convection: Monthly, seasonal, KP, and IMF dependencies. *Journal of Geophysical Research: Space Physics*, *124*(6), 4608–4626. https://doi.org/10.1029/2018JA026268

Maimaiti, M., Ruohoniemi, J. M., Baker, J. B., & Ribeiro, A. J. (2018). Statistical study of nightside quiet time midlatitude ionospheric convection. *Journal of Geophysical Research: Space Physics*, *123*(3), 2228–2240. https://doi.org/10.1002/2017JA024903

Makela, J. J., Meriwether, J. W., Ridley, A. J., Ciocca, M., & Castellez, M. W. (2012). Large-scale measurements of thermospheric dynamics with a multisite Fabry-Perot interferometer network: Overview of plans and results from midlatitude measurements. *International Journal of Geophysics*, *2012*, 1–10. https://doi.org/10.1155/2012/872140

Martin, C. J., Shi, X., Schmidt, M. T., Day, E. K., Bland, E. C., Khanal, K., et al. (2023). pydarn [Software]. *Zenodo*. https://doi.org/10.5281/zenodo.7767590

McHarg, M., Chun, F., Knipp, D., Lu, G., Emery, B., & Ridley, A. (2005). High-latitude joule heating response to IMF inputs. *Journal of Geophysical Research*, *110*(A8), A08309. https://doi.org/10.1029/2004JA010949

Nagano, H., Nishitani, N., & Hori, T. (2015). Occurrence characteristics and lowest speed limit of subauroral polarization stream (SAPS) observed by the superDARN Hokkaido East Radar. *Earth Planets and Space*, *67*(1), 126. https://doi.org/10.1186/s40623-015-0299-7

NCAR. (2016). TIEGCM documentation release 2.0 NCAR high altitude observatory. Retrieved from https://www.hao.ucar.edu/modeling/tgcm/tiegcm2.0/userguide/userguide.pdf

Nishitani, N., Ruohoniemi, J. M., Lester, M., Baker, J. B. H., Koustov, A. V., Shepherd, S. G., et al. (2019). Review of the accomplishments of mid-latitude super dual auroral radar network (SuperDARN) HF radars. *Progress in Earth and Planetary Science*, *6*(1), 27. https://doi.org/10.1186/s40645-019-0270-5

Qian, L., Burns, A. G., Emery, B. A., Foster, B., Lu, G., Maute, A., et al. (2014). The NCAR TIE-GCM (pp. 73–83). https://doi.org/10.1002/9781118704417.ch7

Ribeiro, A. J., Ruohoniemi, J. M., Baker, J. B., Clausen, L. B., Greenwald, R. A., & Lester, M. (2012). A survey of plasma irregularities as seen by the midlatitude Blackstone superDARN radar. *Journal of Geophysical Research*, *117*(A2), A02311. https://doi.org/10.1029/2011JA017207

Ribeiro, A. J., Ruohoniemi, J. M., Baker, J. B., Clausen, L. B., Larquier, S. D., & Greenwald, R. A. (2011). A new approach for identifying ionospheric backscatter in midlatitude superDARN HF radar observations. *Radio Science*, *46*(4), RS4011. https://doi.org/10.1029/2011RS004676

Richmond, A. D., Ridley, E. C., & Roble, R. G. (1992). A thermosphere/ionosphere general circulation model with coupled electrodynamics. *Geophysical Research Letters*, *19*(6), 601–604. https://doi.org/10.1029/92GL00401

Rideout, W., & Coster, A. (2006). Automated GPS processing for global total electron content data. *GPS Solutions*, *10*(3), 219–228. https://doi.org/10.1007/s10291-006-0029-5

Rishbeth, H. (1977). Drifts and winds in the polar F region. *Journal of Atmospheric and Terrestrial Physics*, *39*(1), 111–116. https://doi.org/10.1016/0021-9169(77)90051-4

Rishbeth, H., Moffett, R. J., & Bailey, G. J. (1969). Continuity of air motion in the mid-latitude thermosphere. *Journal of Atmospheric and Terrestrial Physics*, *31*(8), 1035–1047. https://doi.org/10.1016/0021-9169(69)90103-2

Ruohoniemi, J. M., & Baker, K. B. (1998). Large-scale imaging of high-latitude convection with super dual auroral radar network HF radar observations. *Journal of Geophysical Research*, *103*(A9), 20797–20811. https://doi.org/10.1029/98ja01288

Ruohoniemi, J. M., Greenwald, R. A., Baker, K. B., Villain, J.-P., Hanuise, C., & Kelly, J. (1989). Mapping high-latitude plasma convection with coherent HF radars. *Journal of Geophysical Research*, *94*, 13463. https://doi.org/10.1029/ja094ia10p13463

Shepherd, S. G. (2014). Altitude-adjusted corrected geomagnetic coordinates: Definition and functional approximations. *Journal of Geophysical Research: Space Physics*, *119*(9), 7501–7521. https://doi.org/10.1002/2014JA020264

Thomas, E. G., Baker, J. B., Ruohoniemi, J. M., Clausen, L. B., Coster, A. J., Foster, J. C., & Erickson, P. J. (2013). Direct observations of the role of convection electric field in the formation of a polar tongue of ionization from storm enhanced density. *Journal of Geophysical Research: Space Physics*, *118*(3), 1180–1189. https://doi.org/10.1002/jgra.50116

Thomas, E. G., Reimer, A. S., Bland, E. C., Burrell, A. G., Grocott, A., Ponomarenko, P. V., et al. (2022). SuperDARN radar software toolkit (RST) [Software]. *Zenodo*. https://zenodo.org/doi/10.5281/zenodo.801458

Thomas, E. G., & Shepherd, S. G. (2018). Statistical patterns of ionospheric convection derived from mid-latitude, high-latitude, and polar superDARN HF radar observations. *Journal of Geophysical Research: Space Physics*, *123*(4), 3196–3216. https://doi.org/10.1002/2018JA025280

Vasyliunas, V. M., & Song, P. (2005). Meaning of ionospheric joule heating. *Journal of Geophysical Research*, *110*(A2), A02301. https://doi.org/10.1029/2004JA010615

Vierinen, J., Coster, A. J., Rideout, W. C., Erickson, P. J., & Norberg, J. (2016). Statistical framework for estimating GNSS bias. *Atmospheric Measurement Techniques*, *9*(3), 1303–1312. https://doi.org/10.5194/amt-9-1303-2016

Villain, J. P., Greenwald, R. A., Baker, K. B., & Ruohoniemi, J. M. (1987). HF radar observations of E region plasma irregularities produced by oblique electron streaming. *Journal of Geophysical Research*, *92*(A11), 12327–12342. https://doi.org/10.1029/ja092ia11p12327

Wahlund, J. E., Opgenoorth, H. J., Häggström, I., Winser, K. J., & Jones, G. O. L. (1992). EISCAT observations of topside ionospheric ion outflows during auroral activity: Revisited. *Journal of Geophysical Research*, *97*(A3), 3019–3037. https://doi.org/10.1029/91ja02438

Walach, M. T., & Grocott, A. (2019). SuperDARN observations during geomagnetic storms, geomagnetically active times, and enhanced solar wind driving. *Journal of Geophysical Research: Space Physics*, *124*(7), 5828–5847. https://doi.org/10.1029/2019JA026816

Walach, M. T., Grocott, A., & Milan, S. E. (2021). Average ionospheric electric field morphologies during geomagnetic storm phases. *Journal of Geophysical Research: Space Physics*, *126*(4), e2020JA028512. https://doi.org/10.1029/2020JA028512

Wang, X., Miao, J., Aa, E., Ren, T., Wang, Y., Liu, J., & Liu, S. (2020). Statistical analysis of joule heating and thermosphere response during geomagnetic storms of different magnitudes. *Journal of Geophysical Research: Space Physics*, *125*(8), e2020JA027966. https://doi.org/10.1029/2020JA027966

Weimer, D. R. (2005). Improved ionospheric electrodynamic models and application to calculating joule heating rates. *Journal of Geophysical Research*, *110*(A5), A05306. https://doi.org/10.1029/2004JA010884

Wu, Q., Jee, G., Lee, C., Kim, J. H., Kim, Y. H., Ward, W., & Varney, R. H. (2017). First simultaneous multistation observations of the polar cap thermospheric winds. *Journal of Geophysical Research: Space Physics*, *122*(1), 907–915. https://doi.org/10.1002/2016JA023560

Zhang, S. R., Erickson, P. J., Zhang, Y., Wang, W., Huang, C., Coster, A. J., et al. (2017). Observations of ion-neutral coupling associated with strong electrodynamic disturbances during the 2015 St. Patrick's Day storm. *Journal of Geophysical Research: Space Physics*, *122*(1), 1314–1337. https://doi.org/10.1002/2016JA023307

Zhang, X. X., Wang, C., Chen, T., Wang, Y. L., Tan, A., Wu, T. S., et al. (2005). Global patterns of joule heating in the high-latitude ionosphere. *Journal of Geophysical Research*, *110*(A12), A12208. https://doi.org/10.1029/2005JA011222

Zou, Y., & Nishitani, N. (2014). Study of mid-latitude ionospheric convection during quiet and disturbed periods using the SuperDARN Hokkaido radar. *Advances in Space Research*, *54*(3), 473–480. https://doi.org/10.1016/j.asr.2014.01.011